Master's Thesis

Structural Analysis for Flexible Organic Light Emitting Diodes using Finite Element Methods

JiEun Lee

Department of Mechanical Engineering

Graduate School of UNIST

2019

Structural Analysis for Flexible Organic Light Emitting Diodes using Finite Element Methods

JiEun Lee

Department of Mechanical Engineering
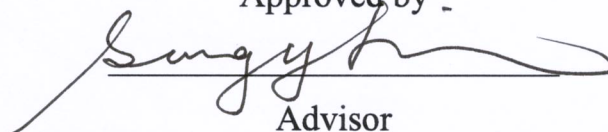
Graduate School of UNIST

Structural Analysis for Flexible Organic Light Emitting Diodes using Finite Element Methods

A thesis/dissertation

submitted to the Graduate School of UNIST

in partial fulfillment of the

requirements for the degree of

Master of Science

JiEun Lee

12. 26. 2018

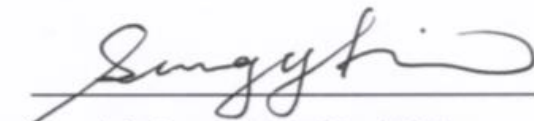Approved by

Advisor

Sung Youb Kim

Structural Analysis for Flexible Organic Light Emitting Diodes using Finite Element Methods

JiEun Lee

This certifies that the thesis/dissertation of JiEun Lee is approved.
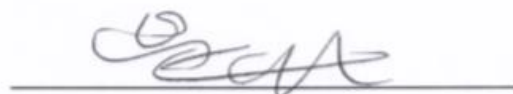
12. 26. 2018

Signature

Advisor: Sung Youb Kim

Signature

Wooseok Ji: Thesis Committee Member #1

signature

Joo Hwan Oh: Thesis Committee Member #2

ABSTRACT

Silver nanowires (AgNWs) electrodes satisfy the conditions that transmittance is higher than 80% at a wavelength of 550 nm and surface resistance is less than 100 $\Omega / \square$, which are required criteria for the application of transparent electrodes. In addition to this, AgNWs have high flexibility and electrical conductivity that are suitable for flexible organic light-emitting diodes (OLEDs), and thus has been of a great interest as an alternative transparent electrode being able to replace indium tin oxide (ITO) of conventional displays.

So far, for the development of alternative transparent electrodes, only transparency and sheet resistance criteria have been considered. However, when we consider flexible display devices in the near future, the transparent electrodes should be robust to folding and stretching in which conventional ITOs have intrinsic limitations. Therefore, a mechanical investigation on the structural stability during folding process is required for the application of AgNWs electrodes to flexible display devices. In this thesis, we performed the stress analysis for OLEDs that contain AgNWs or ITO electrode thin layer as one of components of flexible OLEDs displays. We compared the stress distributions of OLEDs under bending test and investigated the effect of the volume fraction of AgNWs on the structural robustness of the structures.

The first reference model consisted of five layers including ITO with a thickness of 200 nm. Other four layers were aluminum (Al, 70nm), super yellow light-emitting polymer (PDY-132, 80nm), poly (3,4ethylenedioxythiophene) doped with poly (styrene sulfonate) (PEDOT:PSS, 40nm), and polyethylene terephthalate (PET, 0.1mm) layers. The second reference model also consisted of five layers, but now the ITO layer was replaced by AgNWs composite with PEOT:PSS with a thickness of 72 nm while the materials of the other four layers are the same. AgNWs of which length and diameter are 25+-5 um and 36 +-5 nm are employed in real production. Second reference model has a sheet resistance of 12.63 $\Omega / \square$ and a transmittance of 93% at a wavelength of 550 nm.

The real size of the flexible OLED device is 15 mm x 15 mm in the lateral directions, but we carefully reduced it to 7 mm x 1 mm without any significant change in the stress analysis to lower computational cost. We modelled the AgNWs composite layer as a conventional fiber-reinforced composite in which the AgNW acts as a fiber and the conductive polymer PEDOT: PSS acts as a resin. Then we determine the longitudinal Young's modulus (E_L), transverse Young's modulus (E_T), in-plane shear modulus (G_{LT}), and major Poisson's ratio through a proper homogenization. Although AgNWs are arbitrary distributed in the real AgNWs composite layers, we assumed that they are distributed in orthogonal patterns in our numerical models.

AgNWs manufacturing process uses spin-coating. Accurate volume fraction of AgNWs is unknown because the spin rate and time can be changed according to situation or purpose of experiment. However, I can assume that the volume fraction of AgNWs is 10% and the thickness of this layer is twice diameter of AgNW through the SEM images of AgNWs. The Young's modulus and Poisson's ratio of AgNW are 176 GPa, and 0.225. The Young's modulus and Poisson's ratio of PEDOT:PSS are 1.9 GPa and 0.34. For the homogenization for the AgNWs with 10% volume fraction, the values of E_L, E_T, G_{LT} and major Poisson's ratio are 10.81 GPa, 10.87 GPa, 0.85 GPa, and 0.127. As the volume fraction increases from 6% to 65%, the longitudinal Young's modulus also steeply increases from 7.19 GPa to 95.29 GPa.

From the numerical analysis of OLEDs containing ITO or AgNWs with 10% volume fraction, Von-mises distributions in the other four layers such as Al, PDY-132, PEDOT: PSS, and PET layers in the both models were almost the same. However, the maximum Von-mises in the ITO layer, 6.99 GPa was found to be approximately 6.32 GPa larger than the maximum Von-mises in the AgNWs composite layer, 0.67 GPa. In addition to stress distribution, the fracture toughness of ITO and silver are about 2.59 MPa m$^{1/2}$ and 40 MPa m$^{1/2}$ at room temperature. Fracture toughness is used as a failure criterion of material and represents the resistance of the material to brittle fracture. If ITO is used for flexible OLEDs, it will be easy to break even under small deformation. As a result, it was confirmed that the AgNWs electrode is superior to the ITO electrode in the aspect of structural and flexural robustness during bending.

Contents

LIST OF FIGURES

LIST OF TABLES

I. Introduction

1.1 Introduction

As transparent flexible electrodes are developed, flexible devices such foldable displays, wearable devices, and portable medical devices are expected to be commercialized in the near future. For next generation foldable or wearable devices, it is essential to develop electrodes that are transparent, flexible, thin, cheap, and can be made on a large-scale manufacturing process. Indium tin oxide (ITO) which has advantages of low sheet resistance, high transmittance and high work function has been used for conventional displays as transparent electrode. However, ITO has some problems which are high cost, high processing temperature, exclusive production of China, a limited indium resource and low fracture toughness. The most serious problem is ceramic characteristics of ITO. For flexible organic light-emitting diodes (OLEDs), external force is applied to ITO and then the surface is cracked due to its ceramic characteristics. To solve the problems of ITO, various alternative transparent electrodes including carbon nanotubes (CNTs), conducting polymers, metal nanowires(NWs), metal grid, and graphene have recently been developed to replace ITO. Silver nanowires (AgNWs) electrodes satisfy the conditions that transmittance is higher than 80% at a wavelength of 550 nm and sheet resistance is less than 100 $\Omega/\square$, which are required criteria for the application of transparent electrodes. In addition to this, AgNWs have high flexibility and electrical conductivity that are suitable for flexible OLEDs. Therefore, it has been of the greatest interest as an alternative transparent electrode being able to replace ITO of conventional displays.

In the future, transparent electrodes are under stretching or rolling or folding situation. Although transparency and sheet resistance of AgNWs is appropriate for flexible OLEDs instead of ITO, research about stress distribution analysis and fracture is needed. In this thesis, we performed the stress analysis for OLEDs containing AgNWs or ITO layer as an anode of flexible OLED displays. In addition, we compared and analyzed the stress distribution of them in the bending test which has 1 mm radius and investigated the effect of the volume fraction of AgNWs on the structural robustness.

1.2 OLEDs structure and luminescence principle
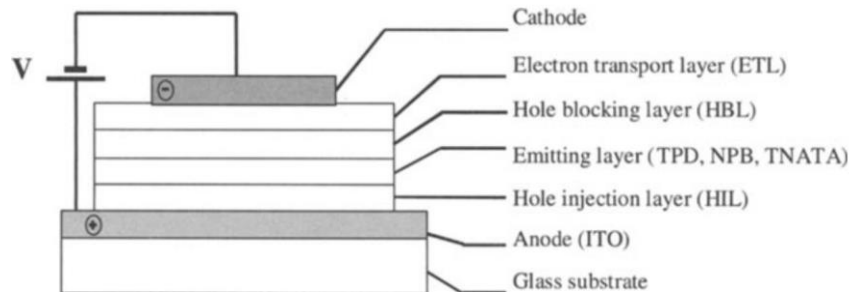
Figure 1-1. The OLEDs layered structure. [6]

OLEDs structure consists of several layers including a substrate, an anode, a hole injection layer (HIL), a hole transport layer (HTL), an emission layer (EML), an electron transport layer (ETL), an electron injection layer (EIL), and a cathode shown in figure 1-1. The reason for using several layers is to improve the luminous efficiency by facilitating the movement of holes and electrons. The layers act like a staircase by lowering the energy barrier. The cathode acts electron injection, and the anode acts hole injection. The HIL is in contact with the anode and roles like a barrier against oxygen, which accelerates the ageing process of the organic layer of EML. It also helps holes to easily reach the EML and need to be transparent to transmit light. HTL is deposited in between the HIL and EML and transfer holes from HIL to the EML. Role of EIL and ETL have same with role of HIL and HTL except for the transfer of electrons instead of holes

Finally, the electrons and holes move to the EML through several layers from cathode and anode. In the EML, they meet and have exciton energy which is very unstable and emits light outward by bandgap. The larger the bandgap, the higher the energy. If organic material used in EML has large bandgap, it will emit blue light with a short wavelength. The other way, EML which has small bandgap emits red light with long wavelength. Since the bandgap is an intrinsic value of organic material, the organic material used in EML determines the light color.

(a)

Transmissive window

Encapsulation substrate

TFT substrate

Image

Transmitted background

(b)

Images

Transmitted background

Encapsulation substrate

TFT substrate

Transmissive window
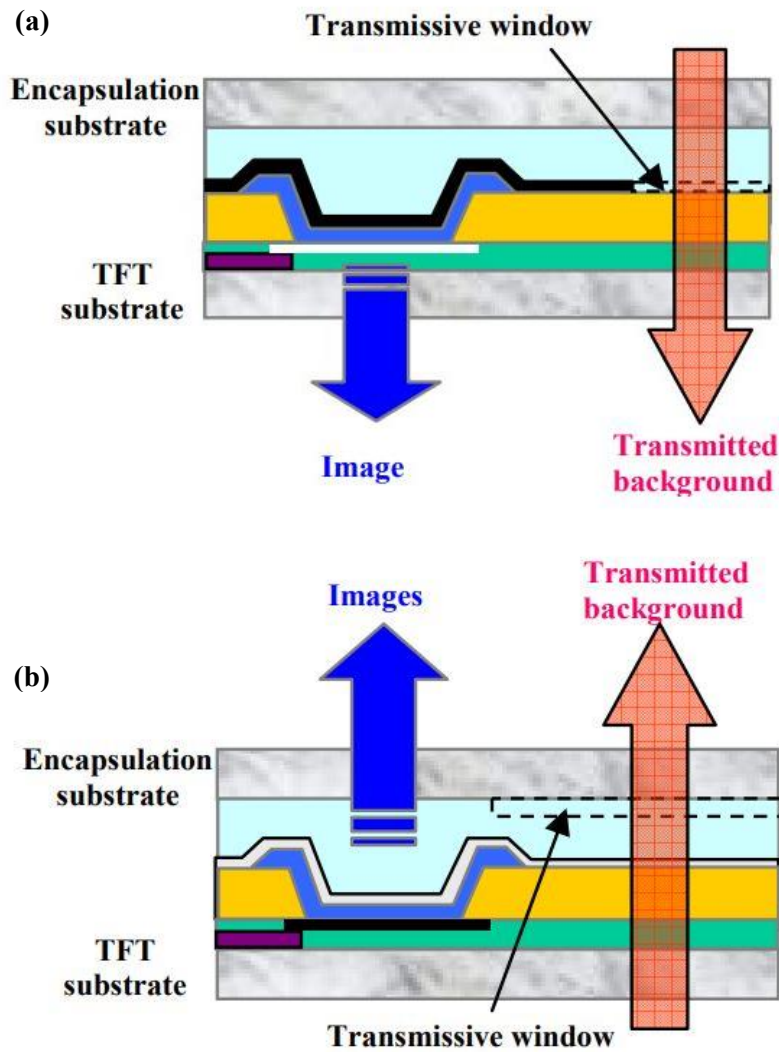
Figure 1-2. Schematic layouts of OLEDs by emission direction. (a) Bottom emission structure. (b) Top emission structure. [7]

It is divided into the top and bottom emission according to the emission direction. In generally, cathode can't emit light because it's made of opaque metal. The light is reflected by the cathode and emitted toward the substrate through the transparent anode. It is called by bottom emission. Figure 1-2 (a) shows the emission direction and the schematic layout of bottom emission. In the bottom emission, the light emitted is partially blocked by a capacitor or a thin film transistor (TFT). It causes low aperture ratio which is the area that can emit light per unit pixel and bad influence on the device life to emit brighter as much as the lost brightness. In the other way, top emission means that the light is emitted toward the cathode. Figure 1-2 (b) shows the emission direction and the schematic layout of the top emission. It has advantages of a high aperture ratio. However, the cathode should be very thin to be transparent, and it causes high sheet resistance and damage of the organic material in the deposition process. In this thesis, we used the bottom emission structure for OLEDs modeling.

1.3 Reference model of OLEDs
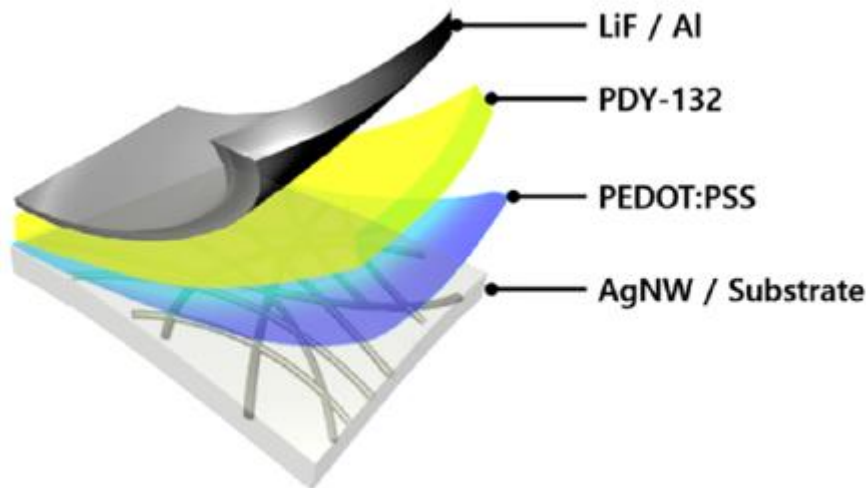
Figure 1-3. The reference model structure of OLEDs containing AgNWs. [1]

There were two reference model of OLEDs containing different transparent electrodes. The first reference model consisted of five layers including ITO with a thickness of 200 nm. Other four layers were aluminum (Al, 70nm), super yellow light-emitting polymer (PDY-132, 80nm), poly (3,4ethylenedioxythiophene) polystyrene sulfonate (PEDOT:PSS, 40nm), and polyethylene terephthalate (PET, 0.1mm) layers. The second reference model also consisted of five layers, but the ITO layer was replaced by AgNWs layer embedded PEDOT:PSS with a thickness of 72 nm and a thickness of PEDOT:PSS was changed from 40 nm to 128 nm, while the materials and thickness of te other three layers are the same. In the reference model shown in figure 1-3, LiF/Al, PDY-132, PEDOT:PSS, AgNWs layer and PET have roles as a cathode, an EML, a HIL, an anode and a substrate. AgNWs used in this model has length 25 ± 5 μm and diameter 36 ± 5 nm. The second reference model has a sheet resistance of 12.63 Ω/□ and a transmittance of 93% at a wavelength of 550 nm. In addition, although an sheet resistance is increased by around 30% after 1200 bending cycles with 1mm radius, it passed bending cycle test.

II. Modeling for Bending Test

2.1 Hinge modeling

2.1.1 Draft modeling
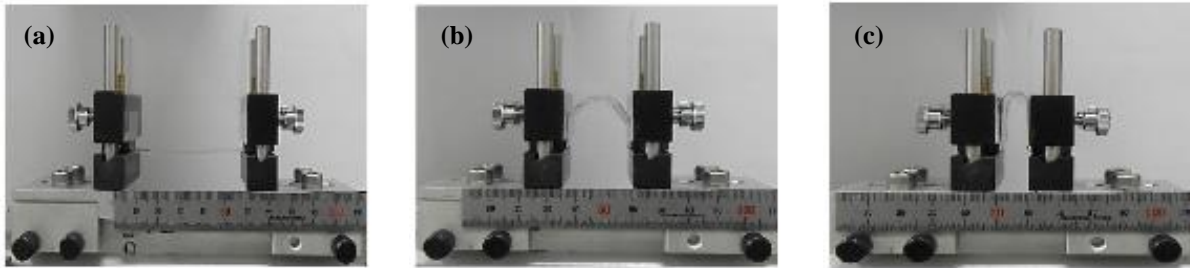
Figure 2-1. Photographs of the bending experiment with a bending radius of (a) ∞ mm, (b) 10 mm and (c) 3.3 mm. [8]
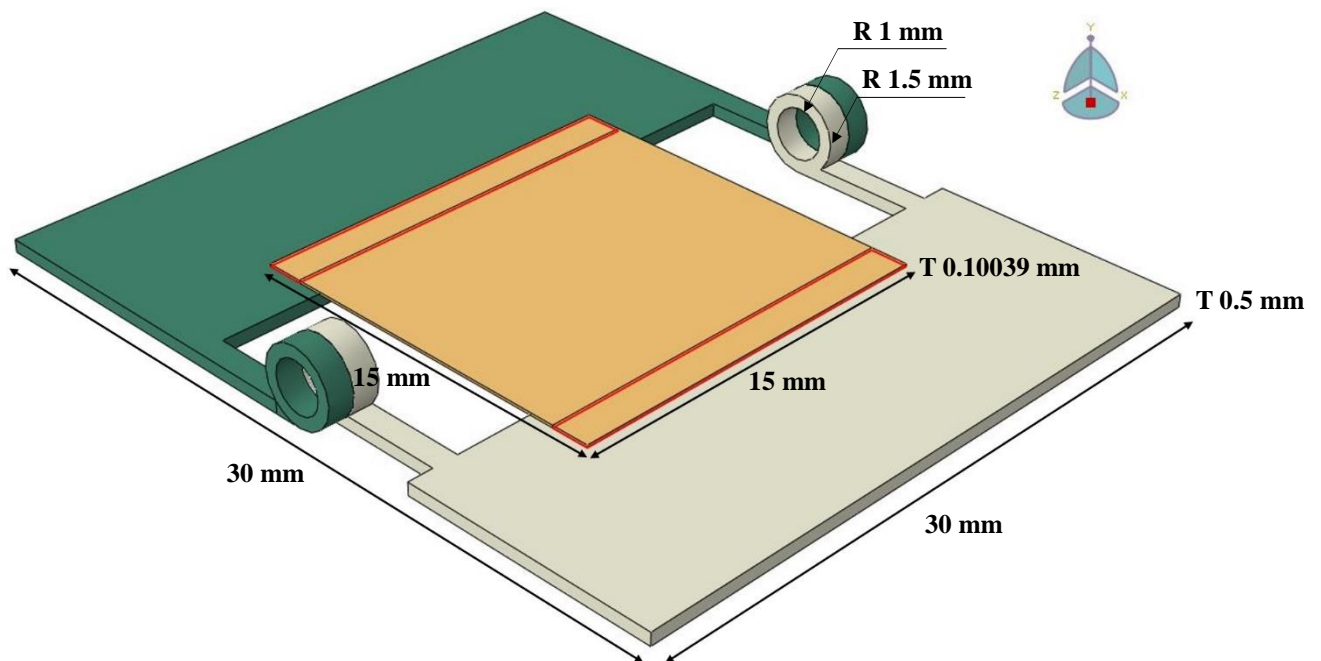
Figure 2-2. Draft modeling for bending test with radius of 1 mm including two hinges and one shell.

The experiment model shown in figure 2-1 has two contact interfaces, where one is fixed, while the other moves horizontally to control the bending radius. In this model, real size of the flexible OLED

and final bending radius is 15 mm × 15 mm and 1 mm. For the structural analysis of flexible OLEDs, a draft modeling for bending test was designed to be a similar with an equipment for bending experiment using ABAQUS. Figure 2-2 shows the designed draft modeling including one shell and two rigid hinges, where left side is fixed, while the right side rotates π radians counterclockwise on a z-axis. The two hinges consist of discrete rigid bodies. The shell consists of composite layup including 5 layers which are Al, PDY-132, PEDOT:PSS, ITO, and PET. In figure 2-2, the red rectangles in the shell are tied on the hinges, and the unbound area contacted with the hinges has a friction.

In ABAQUS, since discrete rigid body doesn't deform under strong forces, it is generally used for press or injection or rolling analyzes and helps less computational time. Element type used in the hinges modeling is R3D4 which is used for a 4-node of 3-dimensional rigid elements. Since the mesh method is not import for rigid body, I determined the mesh size of 0.5 mm. Element type of the shell is S4R which is used for a linear 4-node quadrilateral shell element. Mesh size of the shell is partially different. Global mesh size is 1.5 mm, but mesh size of the length and width is 0.3 mm and 0.2 mm. Element type and mesh are shown in figure 2-3.
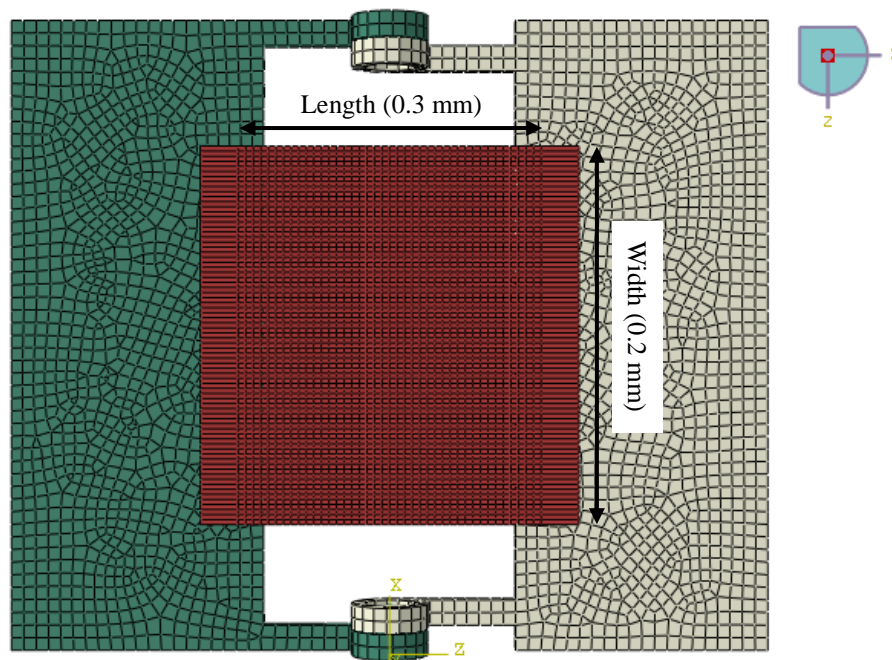
Figure 2-3. Element type and mesh size of the draft modeling.

2.1.2 Support for accurate bending radius
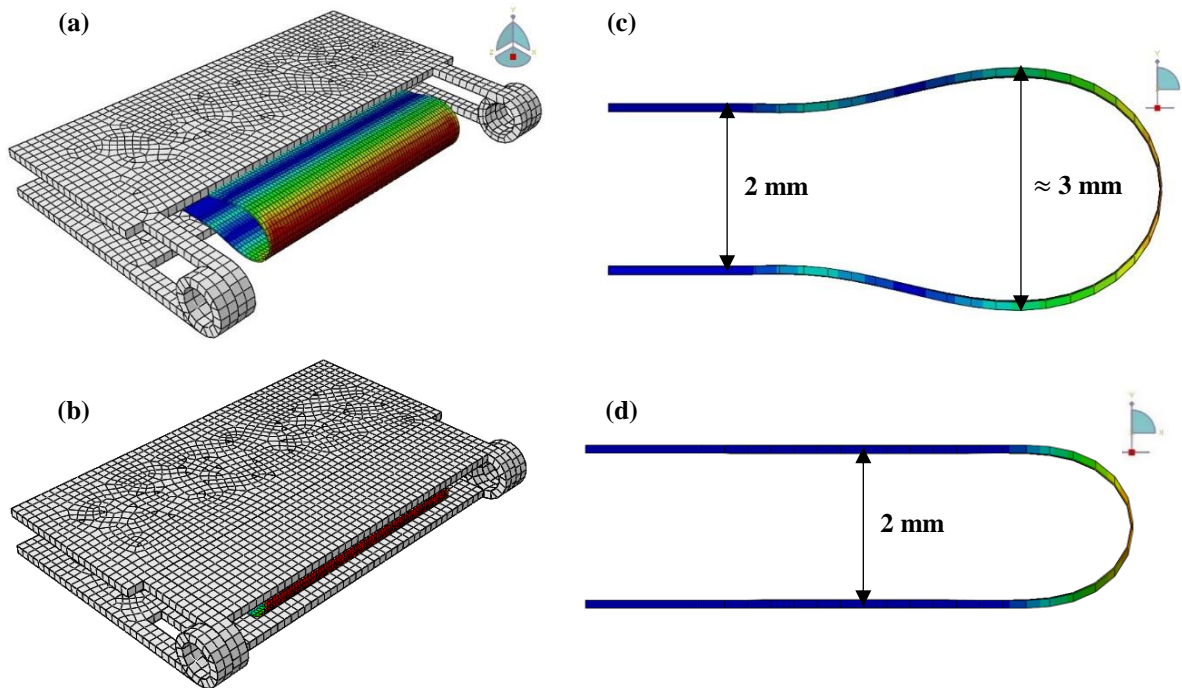
Figure 2-4. For the bending test, hinge modeling in 3-dimension (a) without supports, and (b) with supports. (c) The cross-section of the shell in the x-y plane (c) without supports and (d) with supports.

The shell was tied on the hinges and was bent by rotating of hinge. In the bending test, a hole between the two hinges couldn't induce compressive stress to the shell and the bending radius was changed from 1 mm to about 1.5 mm as shown in figure 2-4 (c). The accurate bending radius couldn't be controlled by the hole. Therefore, I compensated the defect using supports between the hinges like figure 2-4 (b) and the bending radius was controlled to the desired value. Final hinge modeling for bending test is designed as shown in figure 2-5.
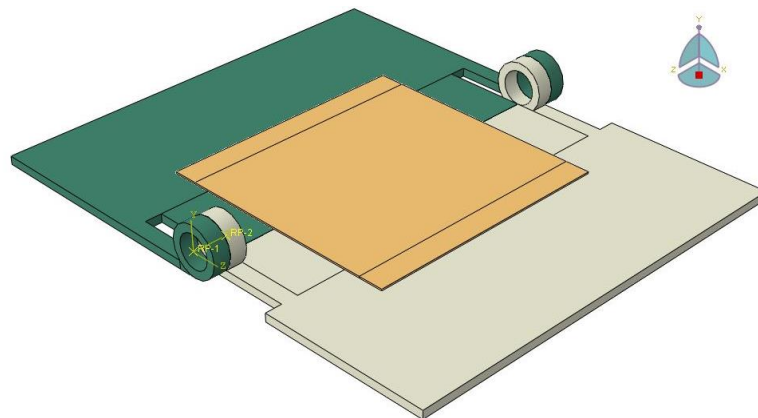
Figure 2-5. The final hinge model with the supports for controlling the accurate bending radius.

2.1.3 Friction between shell and hinges

There was friction in the interface between the unbound area of the shell and the hinges. As the contact area between the hinges and shell increases by support between two hinges, the influence of friction couldn't be ignored. To check the influence of the friction, I changed friction factor from 0.0, 0.3, to 0.9 and then compared Von-mises at the center of shell in each layer. All units of the values listed in table 2-1 are MPa. There is almost no difference by friction factor in each layer. The friction factor doesn't influence on the structural analysis for flexible OLEDs. Therefore, the final hinge modeling shown in the figure 2-5 has the friction factor of 0.3 between the hinges and shell.

Friction factor	0.0	0.3	0.9
Al	3901.42	3906.40	3911.94
PDY-132	377.83	378.31	378.84
PEDOT:PSS	104.97	105.11	105.26
ITO	6429.60	6437.81	6446.95
PET	13.84	13.85	13.83

Table 2-1. The Von-mises values at the center of shell in each layer by friction factor.

2.2 Shell modeling

2.2.1 Reducing width of the shell

(a)
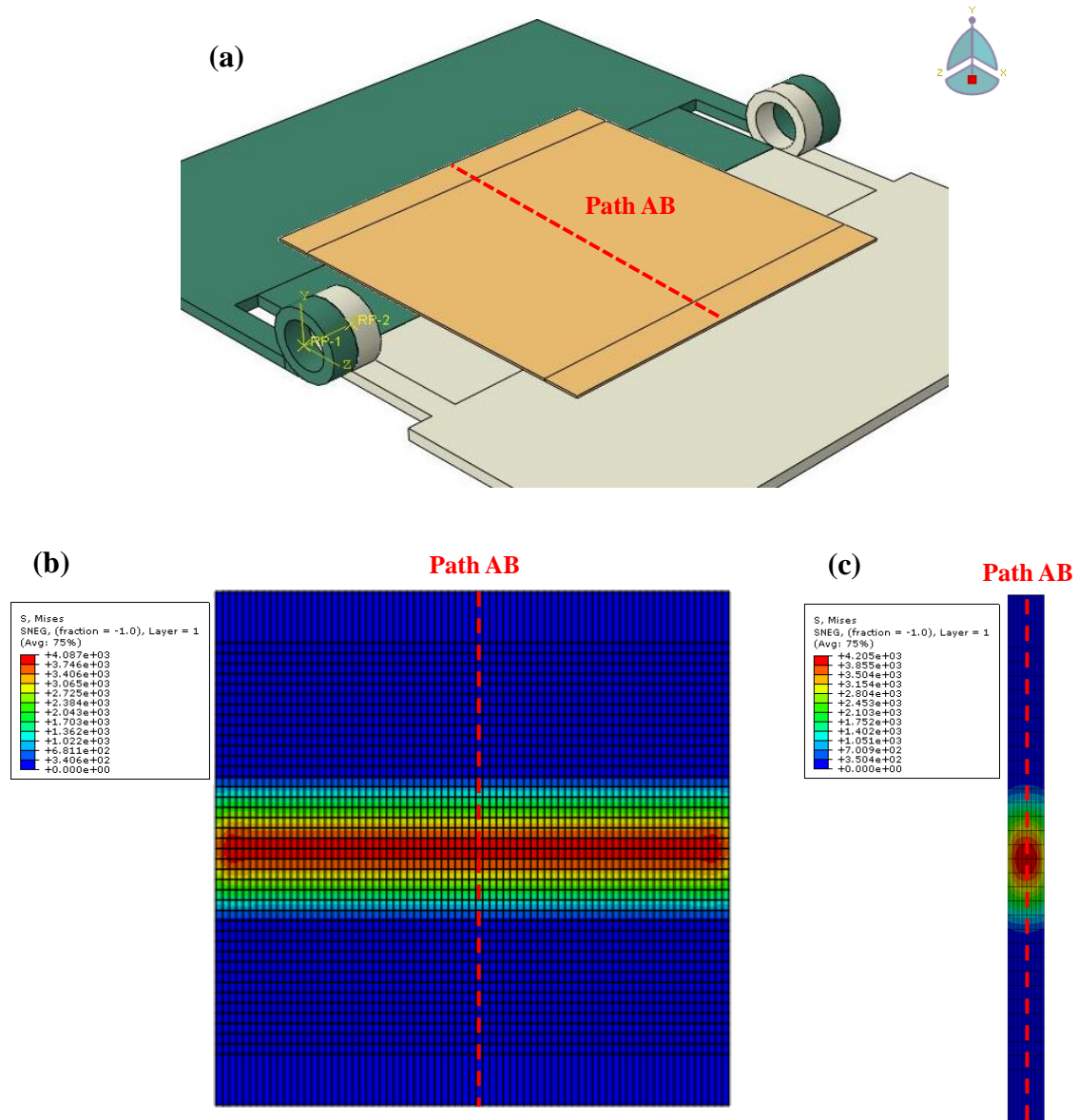
Figure 2-6. (a) There are Path AB along with length of the shell. Von-mises distribution with dimension (b) 15 mm X 15 mm or (c) 15 mm X 1 mm.

For lower computational cost in the structural analysis, size and element number of the shell need to be reduced without any significant stress change. I reduced the width of the shell from 15 mm to 1 mm. In the shell with 15 mm × 15 mm size, 3150 elements have been generated, while the shell with 15 mm × 1 mm had 960 elements with smaller mesh size. The Path AB shown in the figure 2-6 (a) is the half line of the shell width. Figure 2-6 (b) and (c) show Von-mises distribution of the shell in Al layer with 15 mm X 15 mm or 15 mm X 1 mm after bending and the unit is MPa. The values of maximum

Von-mises of the shells are applied at the bent line and almost the same, while there was no stress in the other area. In Al layer, accurate values of Von-mises according to width of the shell are listed in table 2-2.

The figure 2-7 from (a) to (e) shows the result of Von-mises measured at the Path AB in all layers. The values of stress distribution are almost constant despite the change of width of the shell. The gap between maximum stress is about 6.8% and it doesn't affect the results significantly. Therefore, I decided the width of the shell is 1 mm with the least element numbers.

Width [mm]	15	12	10	7	5	1
Maximum Von-mises [GPa]	3.92	3.91	3.91	3.92	3.92	4.20

Table 2-2. Maximum Von-mises at Path AB by reducing width of the shell in Al layer.
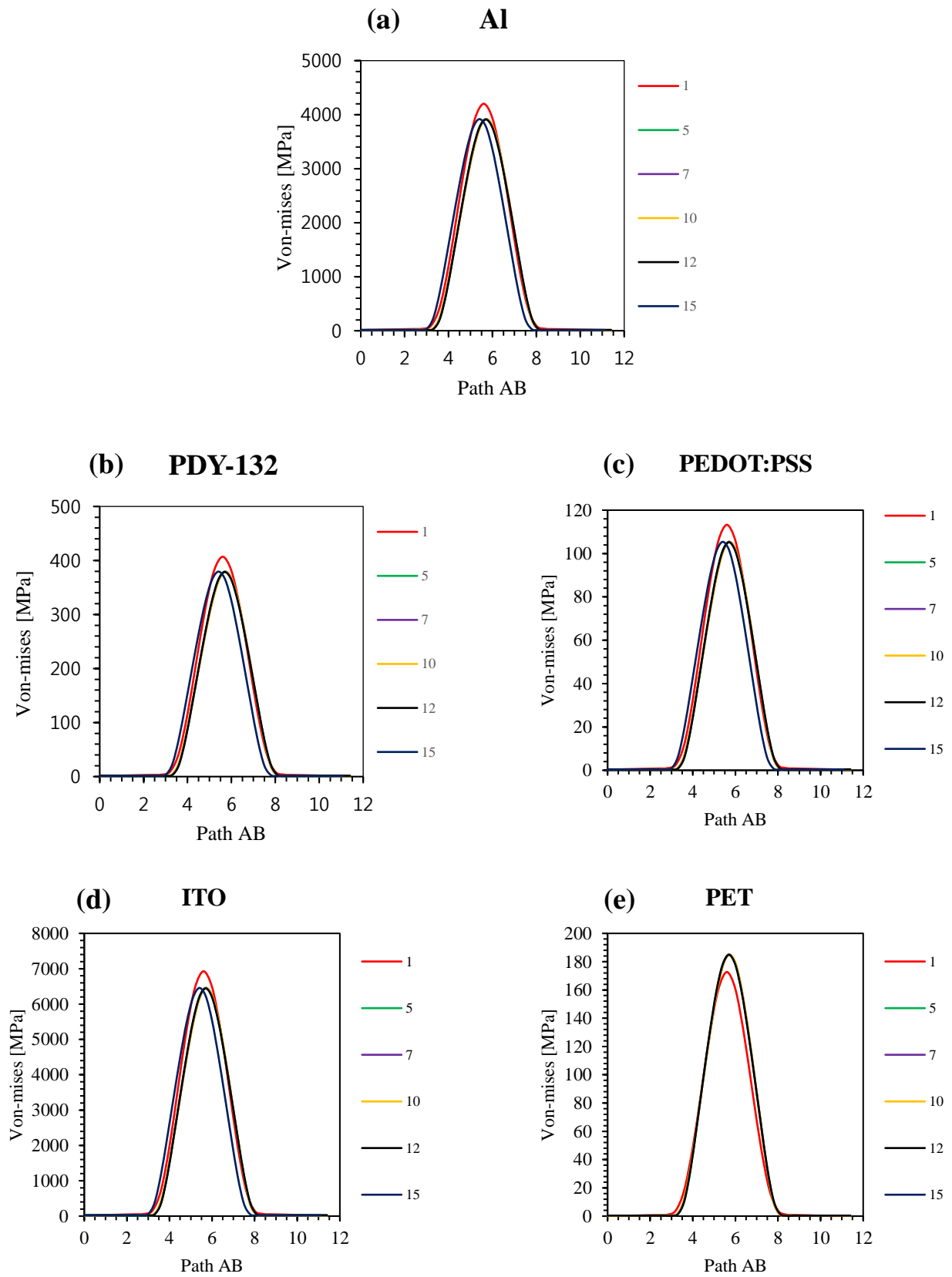
Figure 2-7. The Von-mises result according to Path AB in the (a) Al, (b) PDY-132, (c) PEDOT:PSS, (d) ITO, and (e) PET.

2.2.2 Reducing length of the shell

(a)

Path CD

(b)

```
S, Mises
SNEG, (fraction = -1.0), Layer = 1
(Avg: 75%)
   +4.205e+03
   +3.855e+03
   +3.504e+03
   +3.154e+03
   +2.804e+03
   +2.453e+03
   +2.103e+03
   +1.752e+03
   +1.402e+03
   +1.051e+03
   +7.009e+02
   +3.504e+02
   +0.000e+00
```

Path CD

(c)

```
S, Mises
SNEG, (fraction = -1.0), Layer = 1
(Avg: 75%)
   +4.234e+03
   +3.881e+03
   +3.528e+03
   +3.175e+03
   +2.822e+03
   +2.470e+03
   +2.117e+03
   +1.764e+03
   +1.411e+03
   +1.058e+03
   +7.056e+02
   +3.528e+02
   +0.000e+00
```

Path CD

※ The unit is MPa
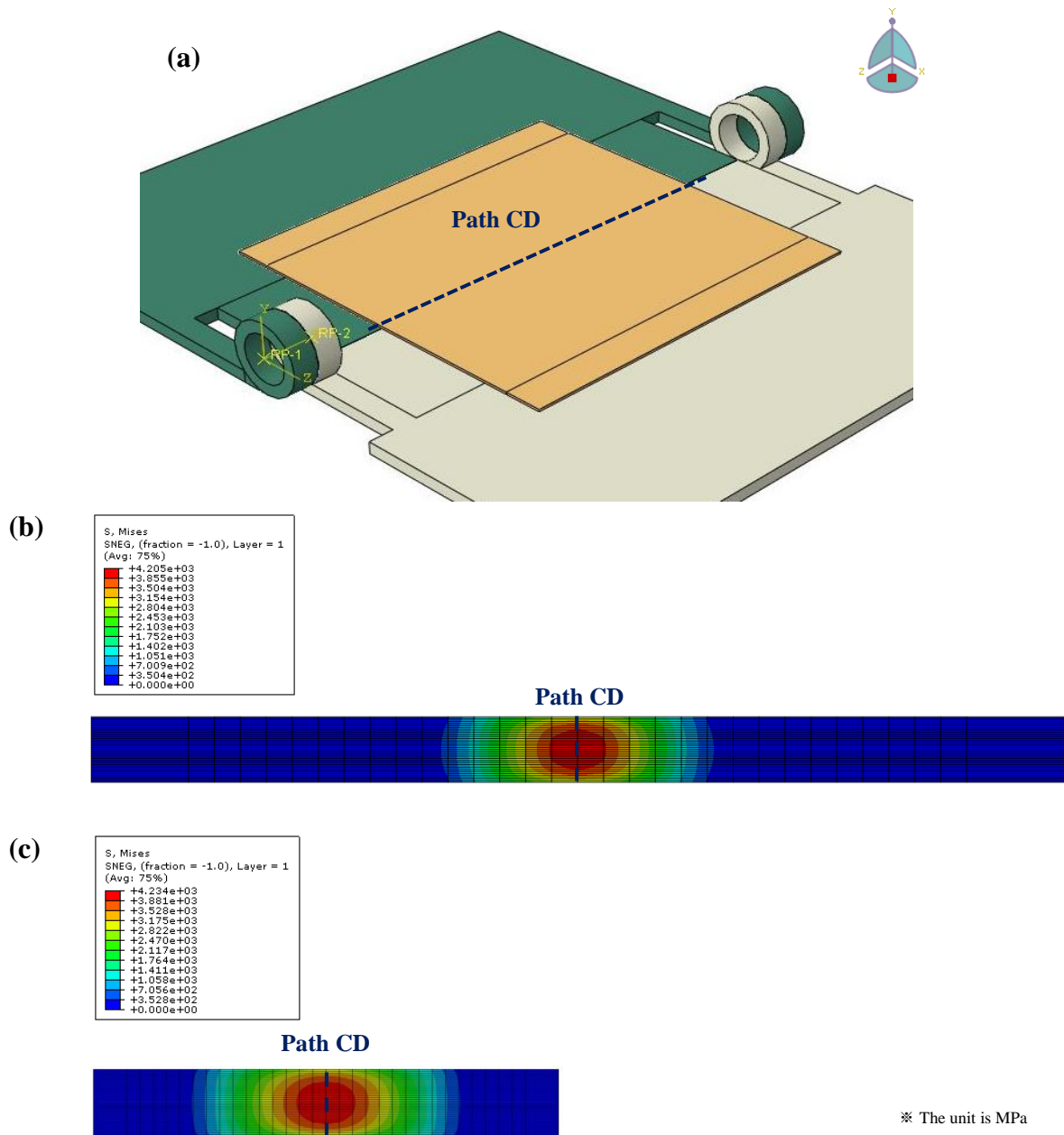
Figure 2-8. (a) There are Path CD at bent line in the shell. Von-mises distribution with dimension (b) 15 mm X 1 mm or (c) 7 mm X 1 mm.

The bent length is about 3.14mm which is equivalent to the length of half circle, because the bending radius is 1 mm. The area near the bent line is influenced by bending stress and the length of the shell should be longer than 5 mm to avoid affecting of the area applied bending stress. As the length of the shell decreases, the fixed area is getting closer to the bent line and free area is getting smaller. It can influence at the stress distribution. I changed the free length from 12 mm to 6 mm with the constant length of the shell, 15 mm and compared the Von-mises result to check the influence. In figure 2-9, the

area in red rectangular is fixed and free length of the figure 2-9 (a) and (b) are 12 mm and 6 mm. Although the free length is different, the result shows similar Von-mises stress distribution in the figure 2-9. Therefore, the free length set at 6 mm regardless of shell length and I reduced the length of the shell from 15 mm to 7 mm, in the same way with reducing width.

Figure 2-8 (b) and (c) show Von-mises distribution of the shell in Al layer with 15 mm X 1 mm or 7 mm X 1 mm after bending. In Al layer, accurate values of the maximum Von-mises according to length of the shell are listed in table 2-3. The Path CD shown in the figure 2-8 (a) is the bent line and applied on the maximum stress. Figure 2-10 (a) – (e) shows the result of Von-mises measured at the Path CD in each layer of shell. The stress distribution is almost constant despite the change of the length. Therefore, the length of the shell set at 7 mm, and the final dimension of the shell was determined as 7 mm × 1 mm. As a result, reduced shell has less mesh size, number of elements and computational time. The detail information is listed in table 2-4.

In the figure 2-11, the dimension of the hinge modeling is same with it of the hinge modeling shown in the figure 2-5, while the dimension of the hinge modeling shown in the figure 2-12 was reduced to match the size of the reduced shell. The final modeling for structural analysis is shown in the figure 2-12.

Length [mm]	15	12	10	7
Maximum Von-mises [GPa]	4.21	4.24	4.23	4.23

Table 2-3. Maximum Von-mises at Path CD by reducing length of the shell in Al layer.

	Shell with 15 mm X 15 mm	Shell with 7 mm X 1 mm
Global Mesh size (length X width) [mm]	1.5 (0.3 X 0.2)	0.5 (0.2 X 0.03)
Number of elements	3150	960
Computational time	29 min	17 min

Table 2-4. Mesh method according dimension of the shell.

(a)

S, Mises
SNEG, (fraction = -1.0), Layer = 1
SPOS, (fraction = 1.0), Layer = 5
(Avg: 75%)
+4.205e+03
+3.855e+03
+3.504e+03
+3.154e+03
+2.804e+03
+2.453e+03
+2.103e+03
+1.752e+03
+1.402e+03
+1.051e+03
+7.009e+02
+3.504e+02
+0.000e+00

(b)

S, Mises
SNEG, (fraction = -1.0), Layer = 1
SPOS, (fraction = 1.0), Layer = 5
(Avg: 75%)
+4.096e+03
+3.755e+03
+3.414e+03
+3.072e+03
+2.731e+03
+2.390e+03
+2.048e+03
+1.707e+03
+1.365e+03
+1.024e+03
+6.827e+02
+3.414e+02
+0.000e+00

※ The unit is MPa
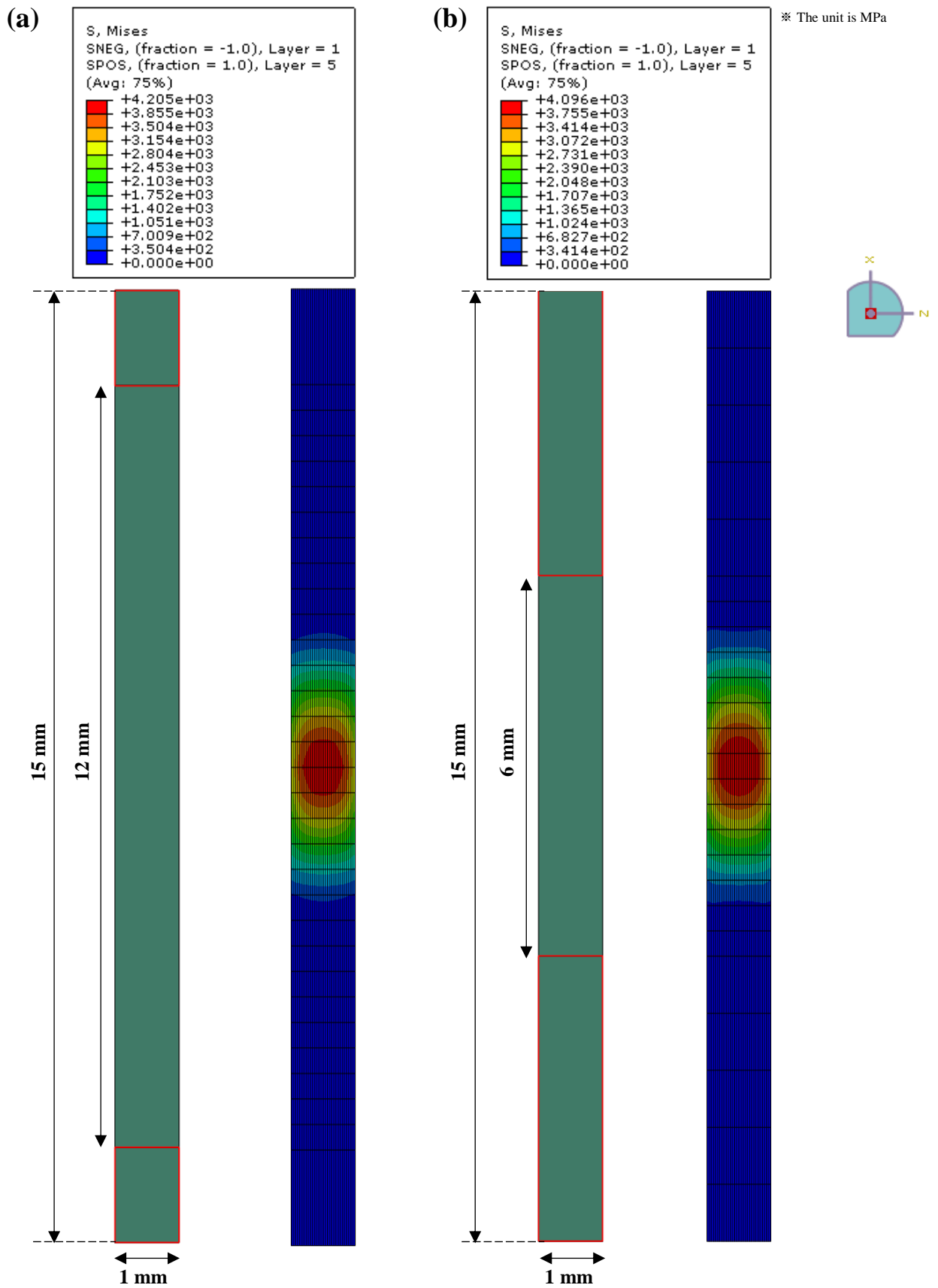
Figure 2-9. The dimension of the bounded shell and Von-mises stress distribution. The free length is (a) 12 mm and (b) 6 mm.
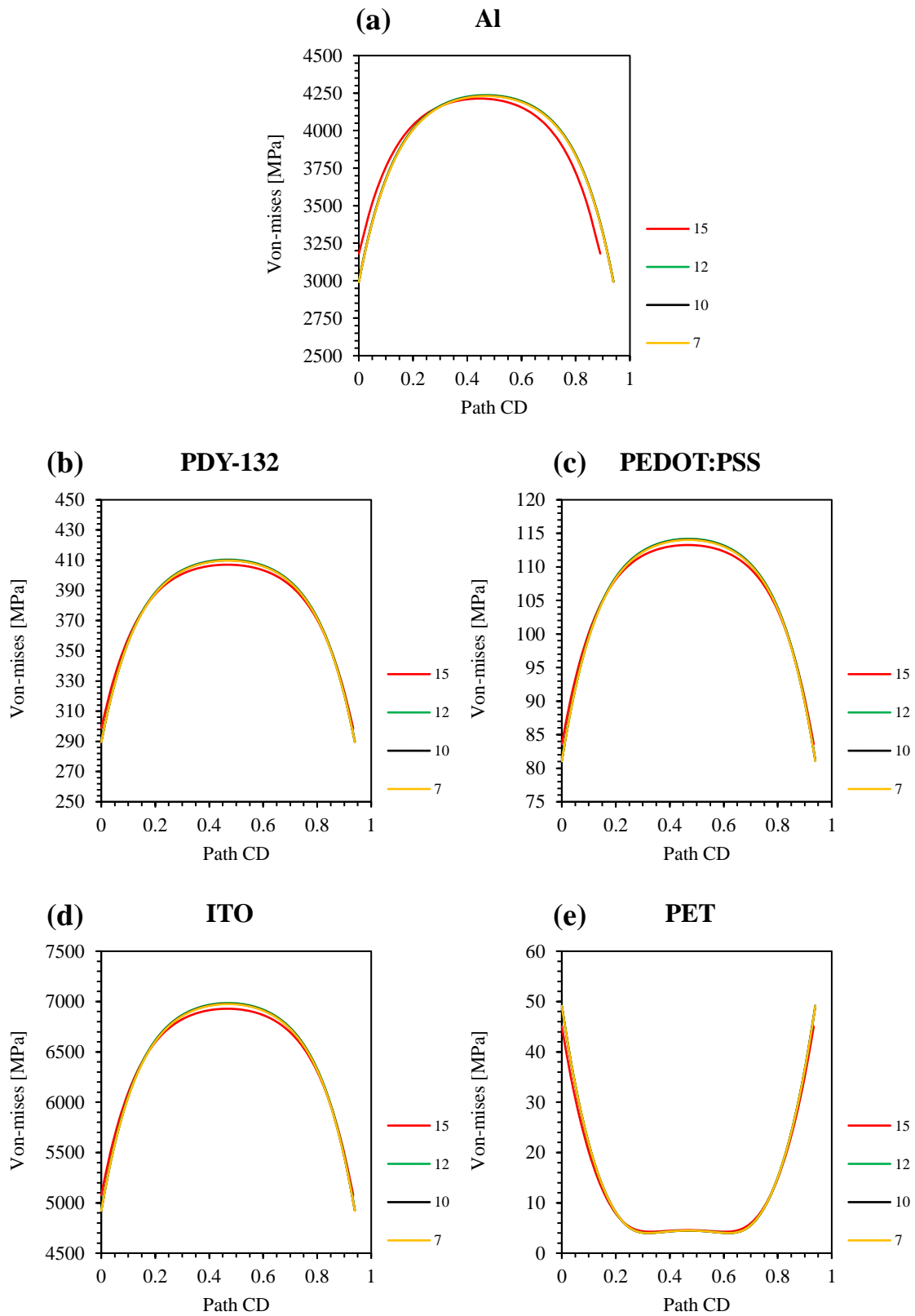
Figure 2-10. The Von-mises result according to Path CD in the (a) Al, (b) PDY-132, (c) PEDOT:PSS, (d) ITO, and (e) PET.

(a)

(b)
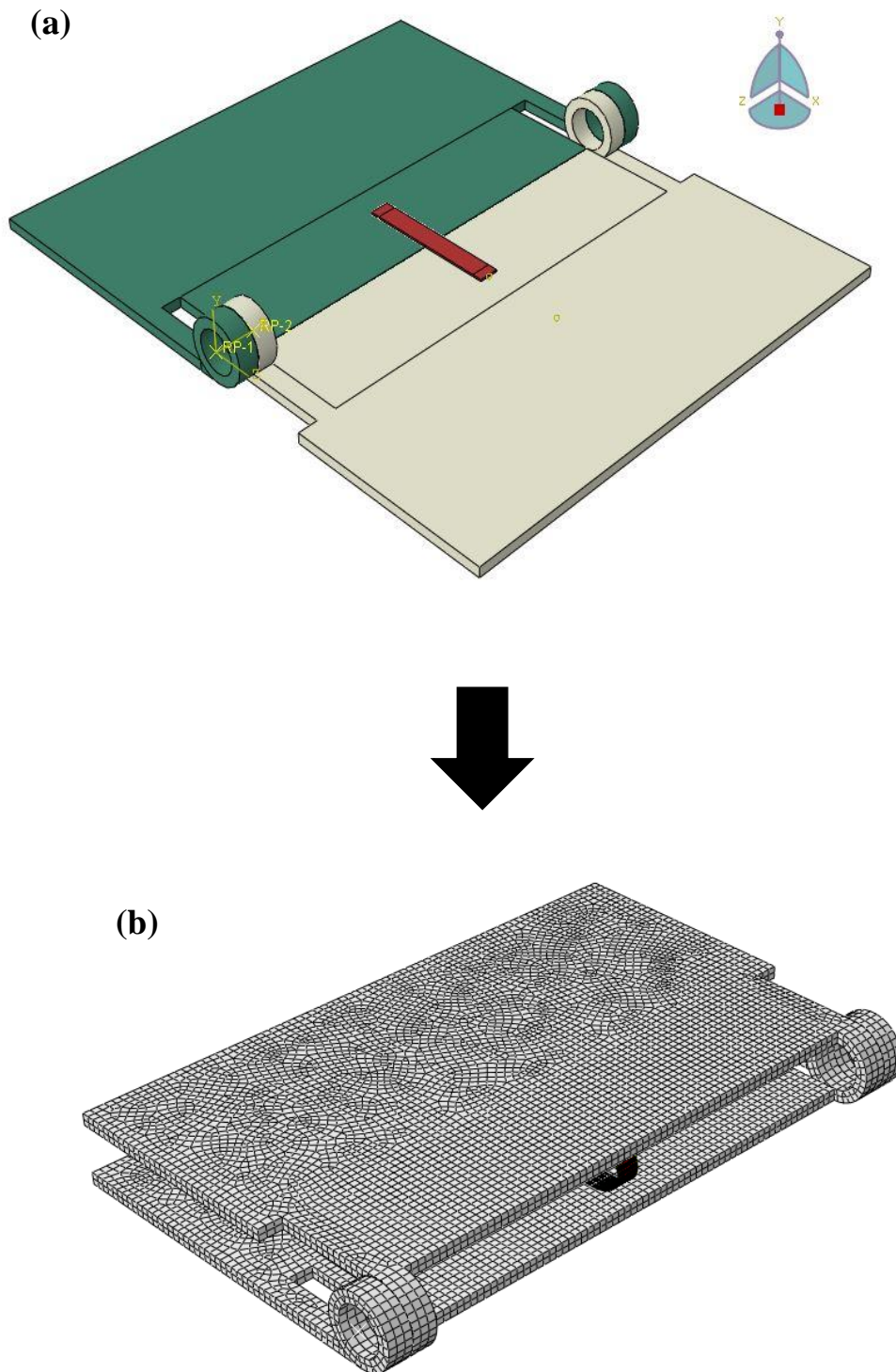
Figure 2-11. (a) and (b) show final modeling before and after bending.

(a)

R 1 mm

R 1.5 mm

Tied Area

7 mm

T 0.5 mm

Friction
factor: 0.3

T 0.10039 mm

1 mm

10 mm

7 mm

(b)
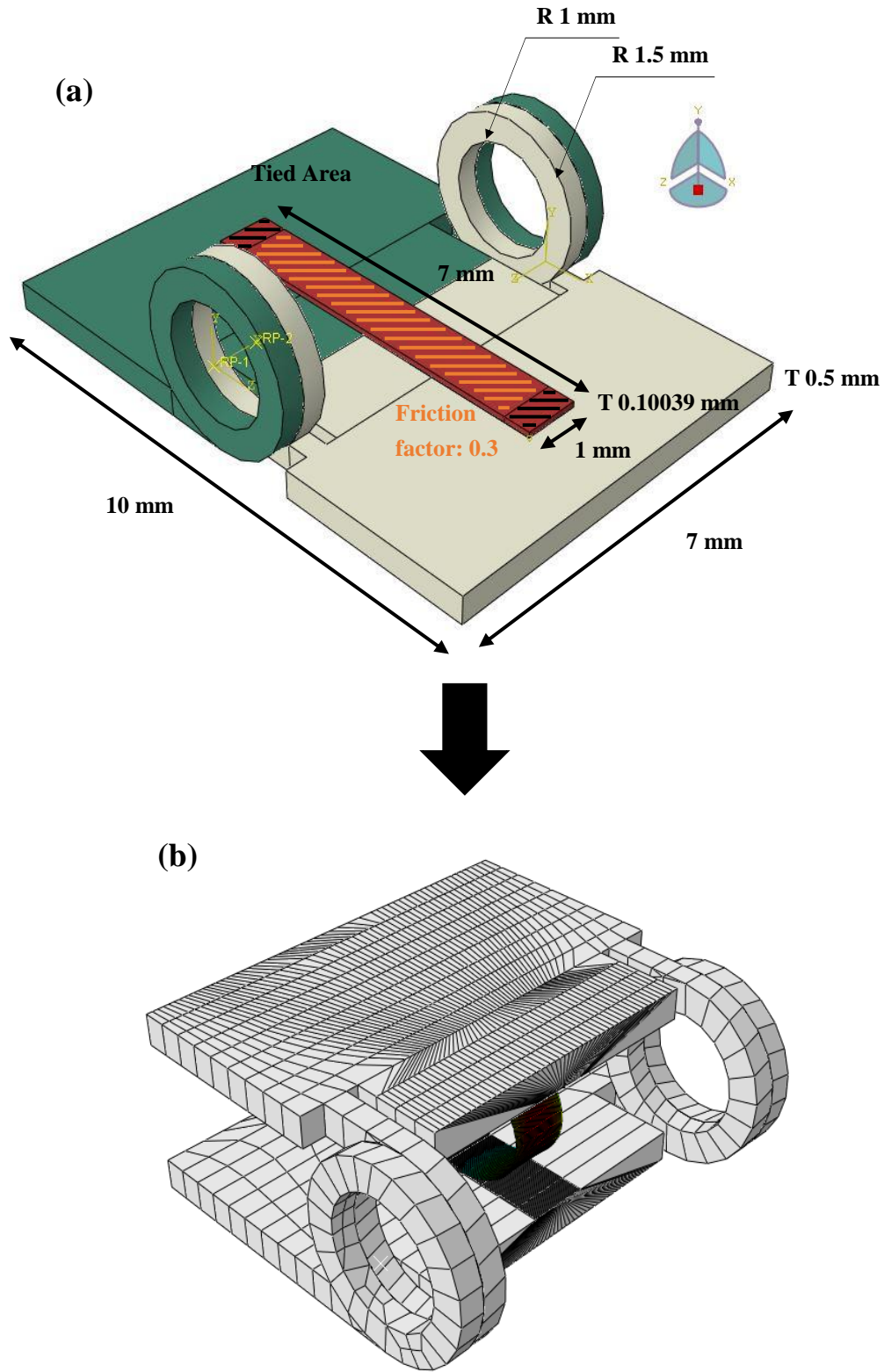
Figure 2-12. (a) and (b) show final modeling with change of hinge size before and after bending.

III.   Homogenization for AgNWs

3.1 Basic concept of homogenization

(a)

Al	— LiF
Super Yellow (PDY-132)	
PEDOT:PSS	
ITO	
PET	

(b)

Material	Thickness [mm]	E [GPa]	ν
Al	7E-5	70	0.35
LiF	1E-6		
PDY-132	8E-5	6.79	0.35
PEDOT:PSS	4E-5	1.9	0.34
ITO	2E-4	116	0.35
PET	0.1	2.8	0.37

(c)

Al	— LiF
Super Yellow (PDY-132)	
PEDOT:PSS	
AgNWs	
PET	

(d)

Material	Thickness [mm]	E [GPa]	ν
Al	7E-5	70	0.35
LiF	1E-6		
PDY-132	8E-5	6.79	0.35
PEDOT:PSS	1.28E-4	1.9	0.34
AgNWs	7.2E-5		
PET	0.1	2.8	0.37
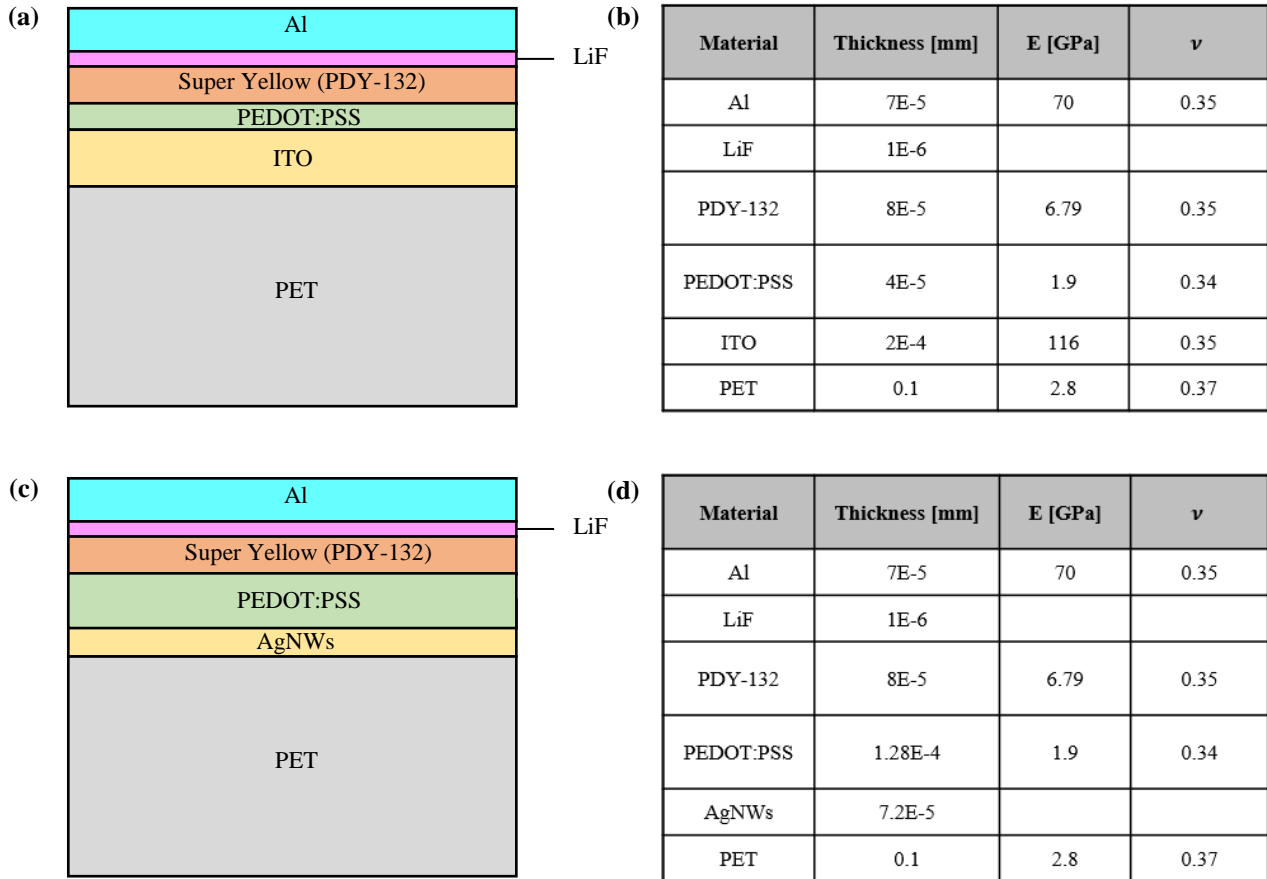
Figure 3-1. (a) The cross section and (b) thickness and mechanical properties of the OLED containing ITO. (c) The cross section and (d) thickness and mechanical properties of the OLED containing AgNWs.

Figure 3-1 shows material and properties of components of the OLED. The difference between the OLED containing ITO or AgNWs are the thickness of PEDOT:PSS and sort of transparent electrode as anode. The AgNWs manufacturing process and the SEM image is shown in figure 3-2. In AgNWs layer, the AgNWs was arbitrary stack on PET using spin-coating and then PEDOT:PSS solution was spin-coated on the top of it. The AgNWs layer consists of AgNWs embedded PEDOT:PSS like a conventional fiber-reinforced composite where the AgNW acts as a reinforcement and the PEDOT:PSS acts as a matrix. The AgNWs give this layer its strength and this layer has directional strength properties according to the oriented AgNWs direction. Although this layer consists two materials, we can get mechanical properties of the composite through a proper homogenization which transforms properties
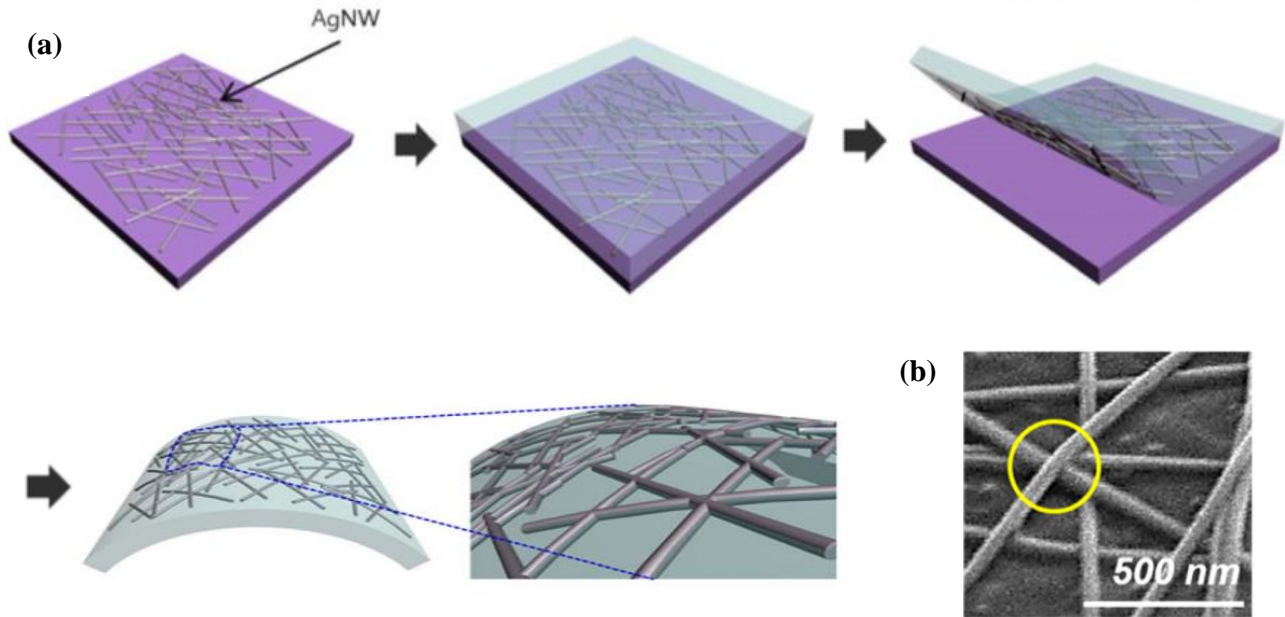
Figure 3-2. (a) Schematic illustration of the AgNWs layer manufacturing process. (b) The SEM image of the AgNWs. [8]

of heterogeneous material into properties of homogeneous continuum. The basic concept of homogenization is that fluctuations that the stress fields at micro-fields influence the macroscopic properties at macro-fields via their volume averages. If the body is sufficiently large, the homogenization can be defined as

$$\bar{\sigma} = \frac{1}{V} \int_V \sigma(x) \, dV$$

where $\bar{\sigma}$, σ, and V for the macroscopic and microscopic stress fields and the volume of the region. Therefore, we can get the properties including the longitudinal Young's modulus (E_L), transversal Young's modulus (E_T), longitudinal shear modulus (G_{LT}), and longitudinal Poisson's ratio (v_{LT}) by calculating properties of the proper reference volume element (RVE) applied on periodic boundary conditions (PBCs) through a homogenization.

3.2 Obtaining the elastic properties

$$\begin{Bmatrix} \bar{\sigma}_{11} \\ \bar{\sigma}_{22} \\ \bar{\sigma}_{33} \\ \bar{\sigma}_{23} \\ \bar{\sigma}_{31} \\ \bar{\sigma}_{12} \end{Bmatrix} = \begin{bmatrix} C_{1111} & C_{1122} & C_{1133} & 0 & 0 & 0 \\ C_{1122} & C_{1111} & C_{1133} & 0 & 0 & 0 \\ C_{1133} & C_{1133} & C_{3333} & 0 & 0 & 0 \\ 0 & 0 & 0 & C_{4444} & 0 & 0 \\ 0 & 0 & 0 & 0 & C_{4444} & 0 \\ 0 & 0 & 0 & 0 & 0 & C_{1212} \end{bmatrix} \begin{Bmatrix} \bar{\varepsilon}_{11} \\ \bar{\varepsilon}_{22} \\ \bar{\varepsilon}_{33} \\ \bar{\varepsilon}_{23} \\ \bar{\varepsilon}_{31} \\ \bar{\varepsilon}_{12} \end{Bmatrix}$$

The relation between stress and strain are related by Hooke's law. C_{ijkl}, σ_{ij} and ε_{ij} are the stiffness tensor, stress tensor and strain tensor. Since the stress and strain tensor is symmetry, the number of independent elastic constants is generally from 81 to 36. Longitudinal fiber reinforced composite is usually assumed transverse isotropy and transversely isotropic material is symmetric about an axis of the fiber. Therefore, the material properties are the same in the direction of the normal plane of the fiber and the number of independent elastic constants is reduced to 5. The elastic properties including longitudinal and transversal Young's modulus (E_L, E_T) and shear modulus (G_{LT}, G_{TT}), and the longitudinal Poisson's ratio (ν_{LT}) is determined by the compliance matrix which is an inverse of the elastic stiffness matrix. The equations for calculation of the elastic properties of transversely isotropic is expressed as

$$E_L = C_{3333} - \frac{2C_{1133}^2}{C_{1111} + C_{1122}}$$

$$E_T = \frac{(C_{1111} - C_{1122}) \times (C_{1111}C_{3333} + C_{1122}C_{3333} - 2C_{1133}^2)}{C_{1111}C_{3333} - C_{1133}^2}$$

$$G_{LT} = C_{4444}$$

$$G_{TT} = C_{1212} = \frac{1}{2}(C_{1111} - C_{1122})$$

$$\nu_{LT} = \frac{C_{1133}}{C_{1111} + C_{1122}}$$

The shear modulus can be defined by Young's modulus and Poisson's ratio as

$$G_{LT} = \frac{E_T}{2(1 + \nu_{TT})}$$

To determine each column of the stiffness tensor of RVE applied PBCs, six analyses are required. When the value of $\bar{\varepsilon}_{kl}$ is 1 and the other all strain tensor values are 0, the value of C_{ijkl} is same with the value of $\bar{\sigma}_{ij}$ which is the volume average of the stress field.

$$\text{When } \bar{\varepsilon}_{kl} = 1, \qquad C_{ijkl} = \bar{\sigma}_{ij} = \frac{1}{V}\int_V \sigma_{ij}\, dV$$

3.3 Analytical method

To calculate the elastic properties of fiber-reinforced composites through analytical method, there are various equations including the Voigt and Reuss, the Hashin-Shtrikman, the Mori-Tanaka, and the Halpin-Tsai method. The simplest equation is the Voigt and Reuss method. The Voigt method assumes a iso-strain model that the strain is everywhere uniform. The equation for this method is expressed as

$$\bar{E} = \frac{\bar{\sigma}}{\bar{\varepsilon}} = \frac{\sum f_i \sigma_i}{\bar{\varepsilon}} = \frac{\sum f_i (\bar{\varepsilon} \cdot E_i)}{\bar{\varepsilon}} = \sum f_i \cdot E_i$$

where the $\bar{E}$, $\bar{\sigma}$, $\bar{\varepsilon}$, f_i, σ_i, and E_i for the macroscopic Young's modulus, macroscopic stress, macroscopic strain, the volume fraction of ith, the microscopic stress and Young's modulus of ith. The volume fraction is the ratio of fiber volume in the entire volume of a composite. It is a very important value in determining elastic properties of the composite and calculated by the simple equation.

$$\text{Volume fraction} = \frac{\text{volume of fibers}}{\text{entire volume of composite}} \times 100 \, [\%]$$

The Reuss method assumes a iso-stress model that the stress is everywhere uniform. The equation for this method is expressed as

$$\bar{E} = \frac{\bar{\sigma}}{\bar{\varepsilon}} = \frac{\bar{\sigma}}{\sum f_i \varepsilon_i} = \frac{\bar{\sigma}}{\sum f_i (\frac{\bar{\sigma}}{E_i})} = \sum \frac{E_i}{f_i}, \quad \therefore \frac{1}{\bar{E}} = \sum \frac{f_i}{E_i}$$

While the elastic properties of composite can be easily calculated by the simple equation of Voigt-Reuss method, the result has large error from the actual values. The Voigt-Reuss method generally determines the range of the elastic properties of the composite, where Voigt and Reuss method is known as the upper-bound and lower-bound of the range.

Among the various method, I used the Halpin-Tsai method for the analytical method which is more accurate than the Voigt and Reuss method. This method is a semi-empirical and helps to calculate the longitudinal and transverse moduli simply. By this method, the equation for the longitudinal Young's modulus and Poisson's ratio are expressed as

$$E_L = E_f V_f + E_m (1 - V_f)$$

$$v_{LT} = v_f V_f + v_m (1 - V_f)$$

where E_f, E_m, v_f, v_m and V_f for the Young's modulus and the Poisson's ratio of fiber and matrix, relatively and the volume fraction of fiber. The equation for the transverse Young's modulus is expressed as

$$E_T = E_m \frac{(1 + \xi \eta_T V_f)}{1 - \eta_T V_f}$$

In this equation, the value of ξ is 2 when the shape of fiber is a circle and the value of η_T can be calculated by the equation.

$$\eta_T = \frac{\frac{E_f}{E_m} - 1}{\frac{E_f}{E_m} + \xi}$$

Finally, the equation for the longitudinal Shear modulus is expressed as

$$G_{LT} = G_m \frac{1 + \xi \eta_G V_f}{1 - \eta_G V_f}$$

where G_m for the Shear modulus of the matrix. The value of ξ is 1 for only a fiber shaped a circle and the value of η_G can be calculated by the equation.

$$\xi = 1 + 40 * V_f^{10}$$

$$\eta_G = \frac{\frac{E_f}{E_m} - 1}{\frac{E_f}{E_m} + \xi}$$

The Young's modulus and Poisson's ratio of fiber and matrix are listed in table 3-1, the homogenization result calculated by the Halpin-Tsai method is listed in table 3-2.

	Fiber	Matrix
Young's Modulus [GPa]	89.9	37.9
Poisson's ratio	0.18	0.18

Table 3-1. The elastic properties of fiber and matrix.

	E_L [GPa]	E_T [GPa]	ν_{LT}	G_{LT} [GPa]	G_{TT} [GPa]
Halpin-Tsai	43.10	41.58	0.18	17.42	17.62

Table 3-2. The elastic properties of the composite calculated by the Halpin-Tsai.

3.4 Periodic boundary conditions

3.4.1 2-dimensional periodic boundary conditions
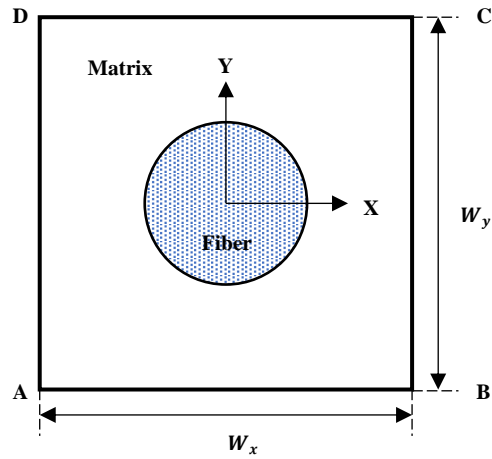
Figure 3-3. Prescribed geometry of 2-dimensional RVE.

2-dimensional (2D) PBCs need two types of node sets including the edge and vertex. It's important to make each set with avoiding overlapping constraints between nodes on the edges and vertices of RVE. All equations for the PBCs should be applied to one node and opposite node on the edges and vertices of the RVE. Figure 3-3 shows the geometry information for the edges and vertices of the RVE to apply 2D PBCs. The constraint equations of 2D PBCs for the edge sets are expressed as

$$u_{BC} - u_{AD} = W_x \varepsilon_x^0$$

$$u_{CD} - u_{AB} = W_y \varepsilon_{yx}^0$$

$$v_{BC} - v_{AD} = W_x \varepsilon_{xy}^0$$

$$v_{CD} - V_{AB} = W_y \varepsilon_y^0$$

Where W_x and W_y are the dimensions of the RVE in the x and y direction and the u and v are the displacement along x and y axis. The constraint equations for the vertex sets are expressed as

$$u_c - u_A = W_x \varepsilon_x^0 + W_y \varepsilon_{yx}^0$$

$$u_B - u_D = W_x \varepsilon_x^0 - W_y \varepsilon_{yx}^0$$

$$v_c - v_A = W_y \varepsilon_y^0 + W_x \varepsilon_{xy}^0$$

$$v_B - v_D = -W_y \varepsilon_y^0 + W_x \varepsilon_{xy}^0$$

3.4.2 3-dimensional periodic boundary conditions
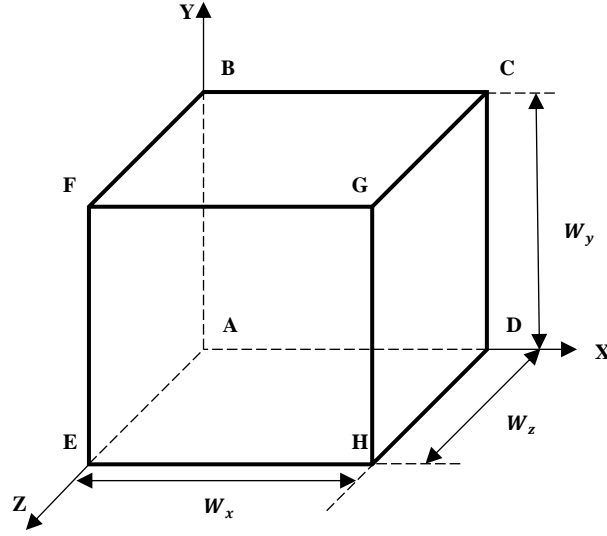
Figure 3-4. Prescribed geometry of 3-dimensional RVE.

Three types of node sets including face, edge, and vertex sets are needed for 3-dimensional (3D) PBCs. For the set, each node of the RVE combines with the node of opposite parallel side. It's important to make each set with avoiding overlapping constraints between nodes on the faces, edges and vertices of RVE in the same way as 2D PBCs. The figure 3-4 shows the geometry information for the faces, edges and vertices of the RVE to apply 3D PBCs. The constraint equations for the face sets are expressed as

$$u_{CDHG} - u_{BAEF} = W_x \varepsilon_x \qquad v_{CDHG} - v_{BAEF} = W_x \varepsilon_{xy} \qquad w_{CDHG} - w_{BAEF} = W_x \varepsilon_{xz}$$

$$u_{EFGH} - u_{ABCD} = W_z \varepsilon_{zx} \qquad v_{EFGH} - v_{ABCD} = W_z \varepsilon_{zy} \qquad w_{EFGH} - w_{ABCD} = W_z \varepsilon_z$$

$$u_{BCGF} - u_{ADHE} = W_y \varepsilon_{yx} \qquad v_{BCGF} - v_{ADHE} = W_y \varepsilon_y \qquad w_{BCGF} - w_{ADHE} = W_y \varepsilon_{yz}$$

Where W_z is the dimensions of the RVE in the z direction and the w represents the displacement along z-axis. The constraint equations for the edge sets are expressed as

$$u_{BC} - u_{EH} = W_y \varepsilon_{yx} - W_z \varepsilon_{zx} \qquad v_{BC} - v_{EH} = W_y \varepsilon_y - W_z \varepsilon_{zy} \qquad w_{BC} - w_{EH} = W_y \varepsilon_{yz} - W_z \varepsilon_z$$

$$u_{CG} - u_{AE} = W_x \varepsilon_x + W_y \varepsilon_{yx} \qquad v_{CG} - v_{AE} = W_x \varepsilon_{xy} + W_y \varepsilon_y \qquad w_{CG} - w_{AE} = W_x \varepsilon_{xz} + W_y \varepsilon_{yz}$$

$$u_{GF} - u_{AD} = W_y \varepsilon_{yx} + W_z \varepsilon_{zx} \qquad v_{GF} - v_{AD} = W_y \varepsilon_y + W_z \varepsilon_{zy} \qquad w_{GF} - w_{AD} = W_y \varepsilon_{yz} + W_z \varepsilon_z$$

$$u_{BF} - u_{DH} = -W_x \varepsilon_x + W_y \varepsilon_{yx} \qquad v_{BF} - v_{DH} = -W_x \varepsilon_{xy} + W_y \varepsilon_y \qquad w_{BF} - w_{DH} = -W_x \varepsilon_{xz} + W_y \varepsilon_{yz}$$

$$u_{HG} - u_{AB} = W_x \varepsilon_x + W_z \varepsilon_{zx} \qquad v_{HG} - v_{AB} = W_x \varepsilon_{xy} + W_z \varepsilon_{zy} \qquad w_{HG} - w_{AB} = W_x \varepsilon_{xz} + W_z \varepsilon_z$$

$$u_{CD} - u_{EF} = W_x \varepsilon_x - W_z \varepsilon_{zx} \qquad v_{CD} - v_{EF} = W_x \varepsilon_{xy} - W_z \varepsilon_{zy} \qquad w_{CD} - w_{EF} = W_x \varepsilon_{xz} - W_z \varepsilon_z$$

The constraint equations for the vertex sets are expressed as

$$u_H - u_B = W_x \varepsilon_x - W_y \varepsilon_{yx} + W_z \varepsilon_{zx}$$

$$u_C - u_E = W_x \varepsilon_x + W_y \varepsilon_{yx} - W_z \varepsilon_{zx}$$

$$u_G - u_A = W_x \varepsilon_x + W_y \varepsilon_{yx} + W_z \varepsilon_{zx}$$

$$u_D - u_F = W_x \varepsilon_x - W_y \varepsilon_{yx} - W_z \varepsilon_{zx}$$

$$v_H - v_B = W_x \varepsilon_{xy} - W_y \varepsilon_y + W_z \varepsilon_{zy}$$

$$v_C - v_E = W_x \varepsilon_{xy} + W_y \varepsilon_y - W_z \varepsilon_{zy}$$

$$v_G - v_A = W_x \varepsilon_{xy} + W_y \varepsilon_y + W_z \varepsilon_{zy}$$

$$v_D - v_F = W_x \varepsilon_{xy} - W_y \varepsilon_y - W_z \varepsilon_{zy}$$

$$w_H - w_B = W_x \varepsilon_{xz} - W_y \varepsilon_{yz} + W_z \varepsilon_z$$

$$w_C - w_E = W_x \varepsilon_{xz} + W_y \varepsilon_{yz} - W_z \varepsilon_z$$

$$w_G - w_A = W_x \varepsilon_{xz} + W_y \varepsilon_{yz} + W_z \varepsilon_z$$

$$w_D - w_F = W_x \varepsilon_{xz} - W_y \varepsilon_{yz} - W_z \varepsilon_z$$

An automatic generation of the symmetric nodes and constraint equations for PBCs needs to be developed because the RVE has lots of nodes. I made a script using the python which automatically numbers at each node and makes the constraint between one node and symmetric node on the opposite side. Since the python script compatible with the ABAQUS which is a commercial software package, it's possible to make easily constraints associated with the PBCs in the ABAQUS by the reading the script.

3.5 Generation of RVE modeling

3.5.1 Generation of RVE modeling with longitudinal pattern of fibers
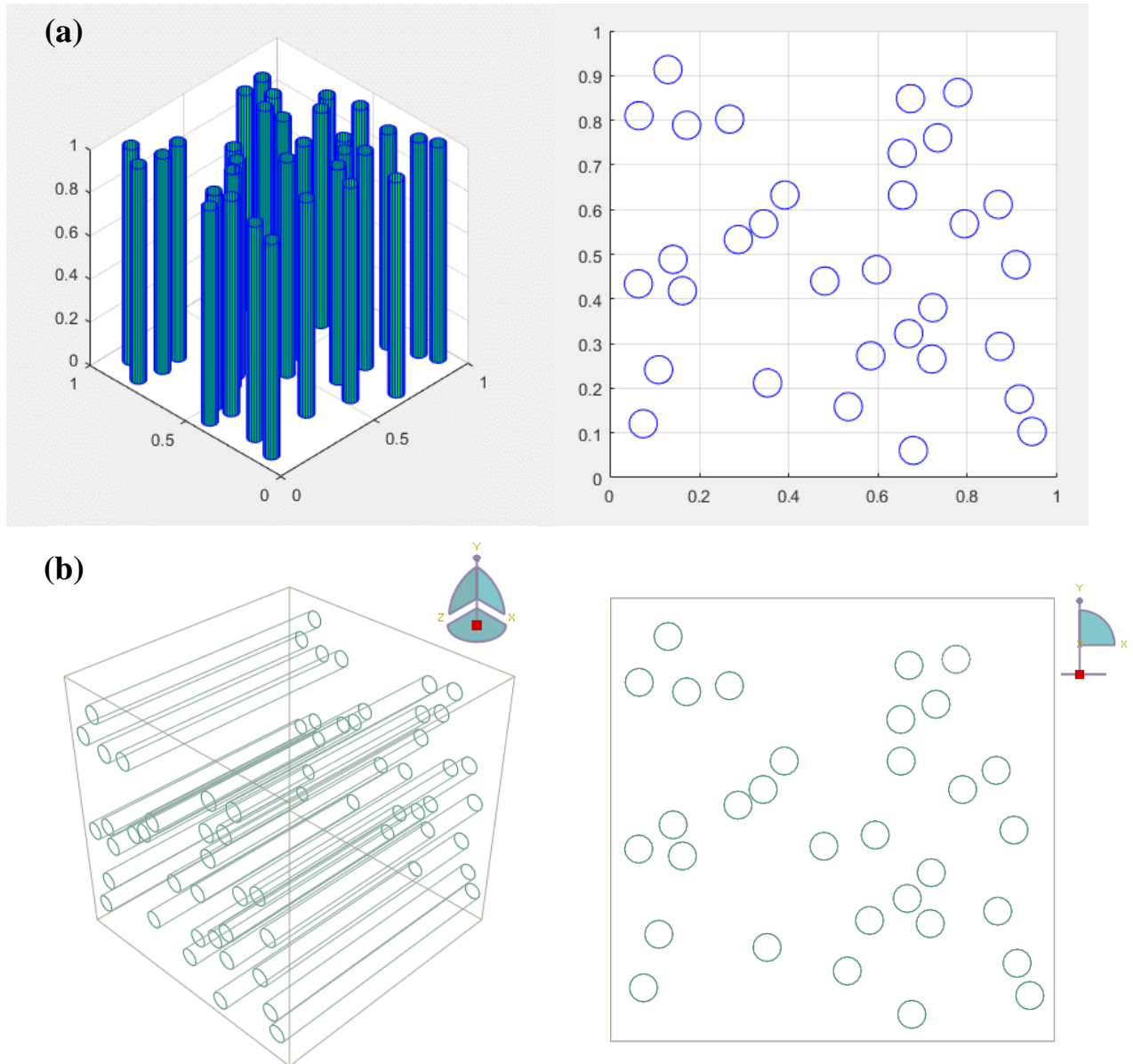
Figure 3-5. The RVE with longitudinal pattern generated random distribution of 32 fibers using (a) MATLAB and (b) ABAQUS.

There are various sorts of fiber in the fiber-reinforced composite according to length, shape, location, orientation and number. First, I assumed the fibers have long length, circle shape, and longitudinal pattern and used the ABAQUS, MATLAB and python programming for generation of RVE modeling.

The contact areas between matrix and fibers perfectly bonded by merging. I made MATLAB and python script to determine automatically the geometrical information of RVE and made the RVE model in ABAQUS by reading the python script which is compatible with ABAQUS. If I input the values of the number of fibers, size of the RVE and volume fraction at the MATLAB script, geometrical information including width, length, and height of the matrix, and radius, length, and randomly location of the fibers were automatically determined and saved in text file. RVE model made by MATLAB is shown in figure 3-5 (a). Python read the geometrical information through the text file and made RVE model shown in figure 3-5 (b) using ABAQUS.

3.5.2 Generation of RVE modeling with orthogonal pattern of fibers
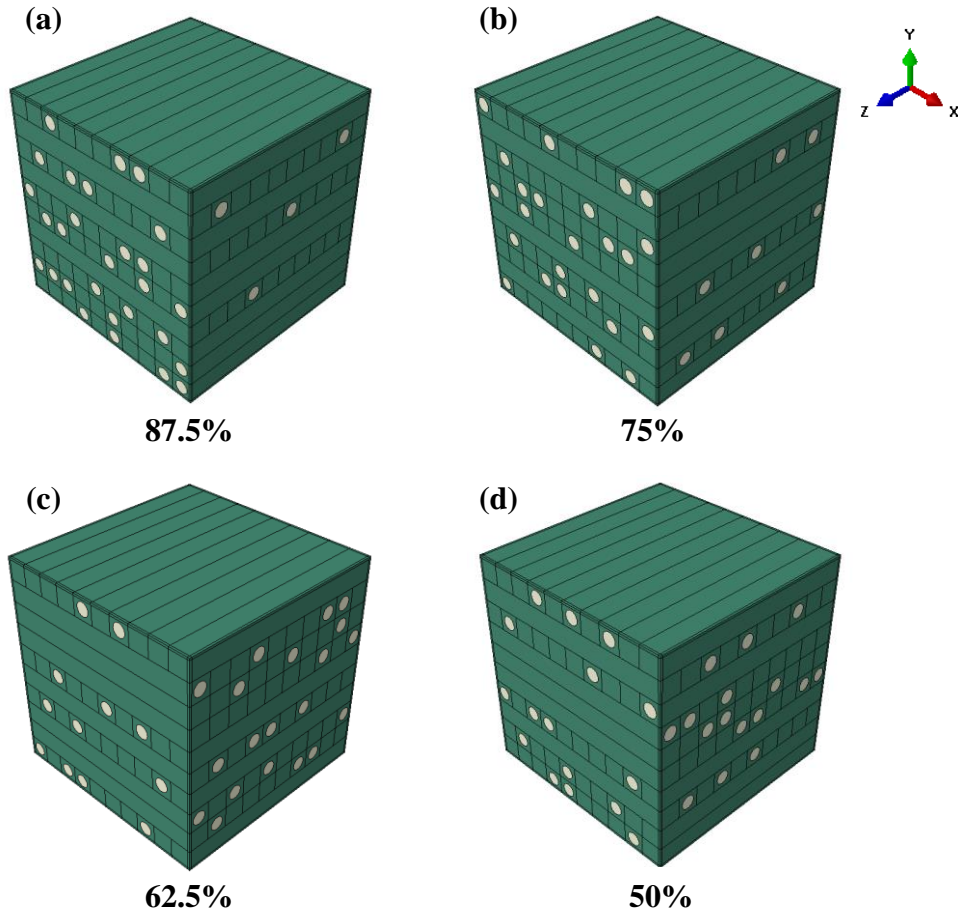
Figure 3-6. The RVE with orthogonal pattern according to fiber ratio on side.

I made python script including geometrical information to make automatically RVE model in ABAQUS. The values of volume fraction, the number of fiber and the size of the composite are 10%, 32, and 10 mm × 10 mm × 10 mm for RVE sample shown in Figure 3-6. Although real model is randomly oriented fiber reinforced composite like the figure 3-2, it's difficult to make the RVE model applied the PBCs. I assumed the fiber has 50 % orthogonal pattern, and the final RVE modeling for homogenization of AgNWs layer is like figure 3-6 (d).

3.6 Comparison between analytical and numerical method

To verify whether the elastic properties obtained through my RVE model applied PBCs is correct, I compared the difference between analytical method and my RVE model. Among the various analytical method, I used the Halpin-Tsai method. The volume fraction of composite is 10%.

Only the value of ε_x is 1 and the other all strain values are 0 ($\varepsilon_x = 1, \varepsilon_y = \varepsilon_z = \gamma_{xy} = \gamma_{yz} = \gamma_{zx} = 0$) in figure 3-7 (a). Likewise, the strain tensor components in figure 3-7 are like that,

(b) : $\varepsilon_y = 1, \varepsilon_x = \varepsilon_z = \gamma_{xy} = \gamma_{yz} = \gamma_{zx} = 0$

(c) : $\varepsilon_z = 1, \varepsilon_x = \varepsilon_y = \gamma_{xy} = \gamma_{yz} = \gamma_{zx} = 0$

(d) : $\gamma_{xy} = 1, \varepsilon_x = \varepsilon_y = \varepsilon_z = \gamma_{yz} = \gamma_{zx} = 0$

(e) : $\gamma_{yz} = 1, \varepsilon_x = \varepsilon_y = \varepsilon_z = \gamma_{xy} = \gamma_{zx} = 0$

(f) : $\gamma_{zx} = 1, \varepsilon_x = \varepsilon_y = \varepsilon_z = \gamma_{xy} = \gamma_{yz} = 0$

As the results, each column of the stiffness matrix is determined and elastic properties of RVE for homogenization also can be determined as shown in the table 3-3. Python script for calculation of the stiffness tesnsor components is shown from the 33 page to 35 page.

The equation for Δ (%) is $\left| \frac{P_{Halphin-Tsai} - P_{numerical}}{P_{Halphin-Tsai}} \right| \times 100$ where the P can be E, ν or G. As results of comparison between analytical and numerical method, the difference average of reference model and my RVE model from values of analytical method are 0.54% and 0.85% which represent very small difference. Therefore, it means that my RVE model is correct for homogenization of composite.

Elastic properties	Analytical method	Reference model [9]		RVE	
		$V_f = 10\%$	Δ (%)	$V_f = 10\%$	Δ (%)
E_L [Gpa]	43.10	-	-	43.06	0.09
E_T [Gpa]	41.58	41.29	0.70	40.86	1.73
ν_{LT}	0.18	0.18	0	0.18	0
G_{LT} [Gpa]	17.42	-	-	17.41	0.07
G_{TT} [Gpa]	17.62	17.46	0.91	17.20	2.38

Table 3-3. Homogenization result calculated by analytical and numerical method and the average difference between analytical and numerical method.

[Python Script for homogenization]

```python
################################################################################
# This script is for homogenization of case1

from odbAccess import *
from abaqus import *
from abaqusConstants import *
import visualization
import sys

myViewport = session.Viewport(name='Viewport: 1',origin=(0, 0), width=150, height=100)
session.viewports['Viewport: 1'].makeCurrent()
session.viewports['Viewport: 1'].maximize()

odb1 = visualization.openOdb (path='case1.odb')    # reading 'case1.odb' file
myAssembly = odb1.rootAssembly
myViewport.setValues(displayedObject=odb1)

loadlist = [0,1,2,3,4,5]
txtlist1 = [0,1,2]
txtlist2 = [5,4,3]
#0 for normal x direction
#1 for normal y direction
#2 for normal z direction
#3 for shear xy direction
#4 for shear yz direction
#5 for shear xz direction
element_type = ['C3D8R']

step1 = odb1.steps['Step-1']
list_macroscopic_stress1 = []
currentFrame = step1.frames[-1]    # frames[-1]=frames[FinalStep]=frames[10]
```

```python
myregion = myAssembly.elementSets[' ALL ELEMENTS']


save_macroscopic_stress = 0

save_temp_vol = 0

stressField = currentFrame.fieldOutputs['S']

ivolField = currentFrame.fieldOutputs['IVOL']    # IVOL = IntegraionPointVolume


field = stressField.getSubset(region = myregion, position = INTEGRATION_POINT, elementType = 'C3D8R')

fieldValues_stress = field.values

field = ivolField.getSubset(region = myregion, position = INTEGRATION_POINT, elementType = 'C3D8R')

fieldValues_ivol = field.values


for loadtype in loadlist:


    counter = 0

    temp_vol = 0

    temp_stress_times_vol = 0


    for v in fieldValues_stress:

        temp_vol = temp_vol + fieldValues_ivol[counter].data

        temp_stress_times_vol=temp_stress_times_vol+.data[loadtype]*fieldValues_ivol[counter].data

        counter = counter + 1


    macroscopic_stress = temp_stress_times_vol/temp_vol

    list_macroscopic_stress1.append(macroscopic_stress)
########################################################################################
# repeat the process of case2, 3, 4, 5, and 6 and get the list_macroscopic_stress2, 3, 4, 5, and 6


output_file = open('homogenized_stiffeness_output.txt','w')

for i in txtlist1:

    output_file.write('%16.8E \t %16.8E \t %16.8E \t %16.8E \t %16.8E \t %16.8E \n' % (

        list_macroscopic_stress1[i], list_macroscopic_stress2[i], list_macroscopic_stress3[i],
```

```
        list_macroscopic_stress4[i], list_macroscopic_stress5[i], list_macroscopic_stress6[i]))
output_file.close()


output_file = open('homogenized_stiffeness_output.txt','a')
for i in txtlist2:
    output_file.write('%16.8E \t %16.8E \t %16.8E \t %16.8E \t %16.8E \t %16.8E \n' % (
        list_macroscopic_stress1[i], list_macroscopic_stress2[i], list_macroscopic_stress3[i],
        list_macroscopic_stress6[i], list_macroscopic_stress5[i], list_macroscopic_stress4[i]))
output_file.close()


###################################################################################################
# Through the 'homogenized_stiffeness_output.txt', we can get the stiffness tensor and then calculate the elastic
properties of the composite
```

(a)

S, Mises
(Avg: 75%)
+4.374e+04
+4.179e+04
+3.984e+04
+3.789e+04
+3.594e+04
+3.399e+04
+3.204e+04
+3.009e+04
+2.814e+04
+2.619e+04
+2.424e+04
+2.229e+04
+2.034e+04

(b)

S, Mises
(Avg: 75%)
+4.373e+04
+4.177e+04
+3.982e+04
+3.786e+04
+3.591e+04
+3.395e+04
+3.200e+04
+3.004e+04
+2.809e+04
+2.613e+04
+2.418e+04
+2.222e+04
+2.027e+04

(c)

S, Mises
(Avg: 75%)
+8.208e+04
+7.790e+04
+7.371e+04
+6.952e+04
+6.534e+04
+6.115e+04
+5.696e+04
+5.278e+04
+4.859e+04
+4.440e+04
+4.022e+04
+3.603e+04
+3.185e+04

(d)

S, Mises
(Avg: 75%)
+3.473e+04
+3.401e+04
+3.329e+04
+3.256e+04
+3.184e+04
+3.112e+04
+3.039e+04
+2.967e+04
+2.895e+04
+2.823e+04
+2.750e+04
+2.678e+04
+2.606e+04

(e)

S, Mises
(Avg: 75%)
+4.095e+04
+3.912e+04
+3.728e+04
+3.545e+04
+3.361e+04
+3.178e+04
+2.994e+04
+2.811e+04
+2.627e+04
+2.444e+04
+2.260e+04
+2.077e+04
+1.893e+04

(f)

S, Mises
(Avg: 75%)
+4.108e+04
+3.924e+04
+3.739e+04
+3.555e+04
+3.371e+04
+3.186e+04
+3.002e+04
+2.818e+04
+2.633e+04
+2.449e+04
+2.265e+04
+2.081e+04
+1.896e+04
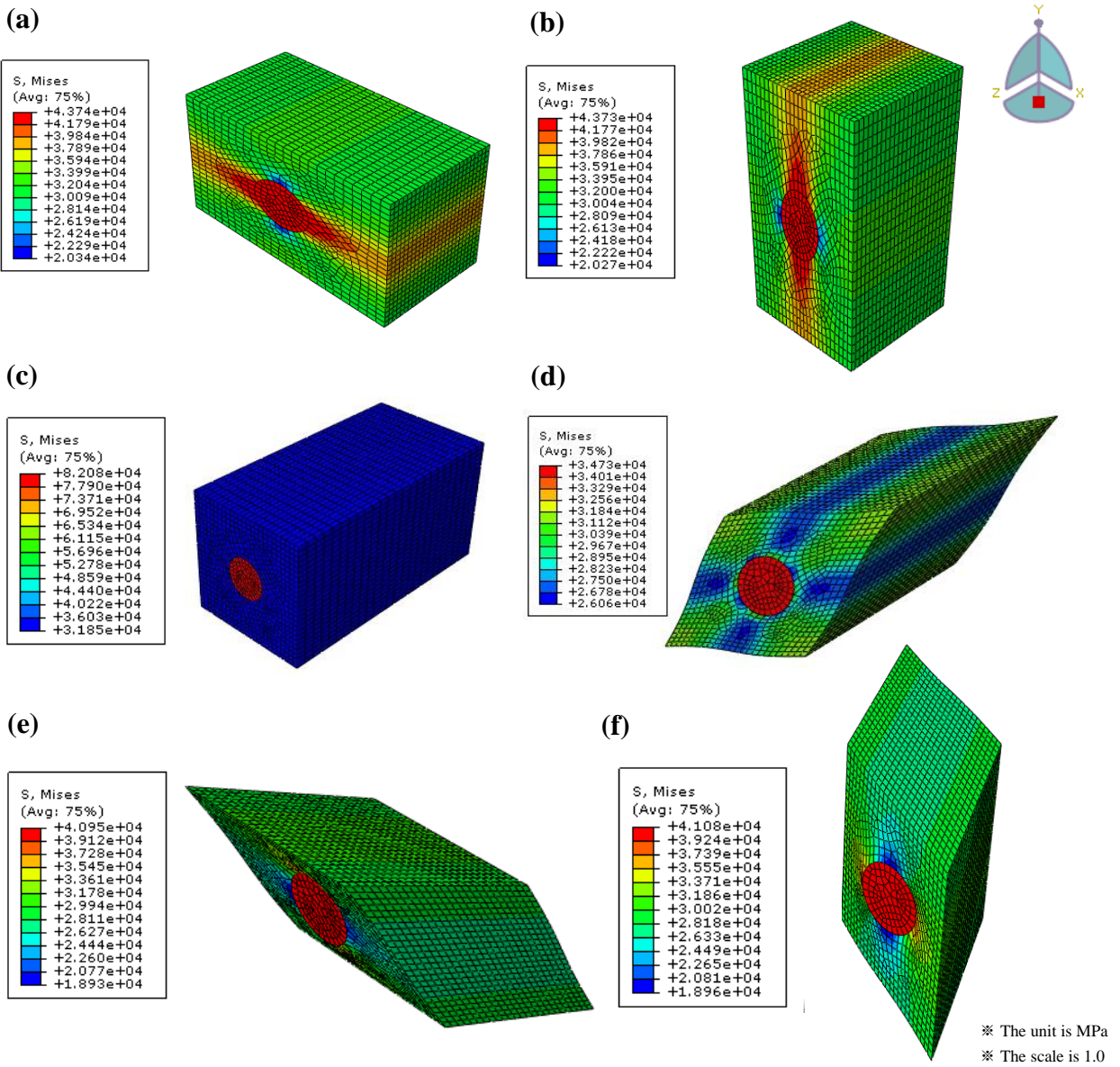
※ The unit is MPa
※ The scale is 1.0

Figure 3-7. The stress distribution of RVE according to component of strain tensor.

3.7 Influence by fibers on homogenization result

3.7.1 Influence by number of fibers
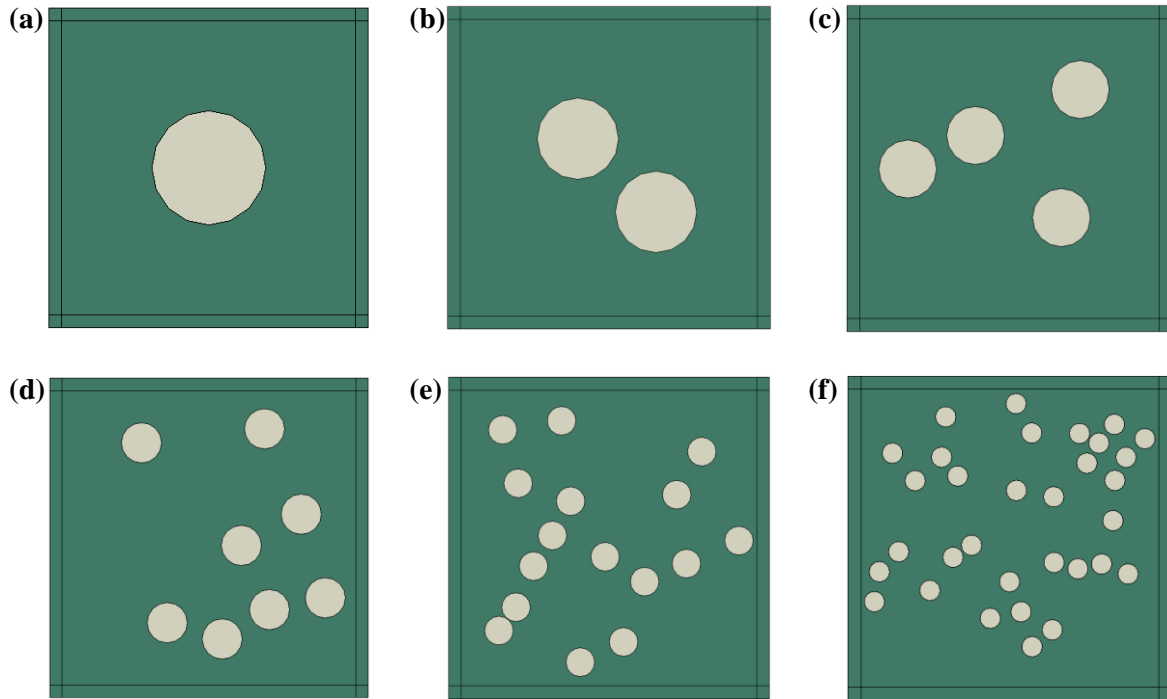
Figure 3-8. The cross-section of composite according to the number of fibers of (a) 1, (b) 2, (c) 4, (d) 8, (e) 16, and (f) 32 with constant volume fraction, 10%.

Since the exact number of AgNWs is unknown, I had to select an arbitrary number of fibers and checked the influence according to the number of fibers on homogenization result. I changed the number of fibers from 1 to 32 with longitudinal pattern and constant volume fraction, 10%. Position of the fibers are randomly distributed as shown in figure 3-8. The elastic properties of fiber and matrix are same with values listed in the table 3-1 and used analytical method for comparison from numerical method is the Halphin-Tsai method. Homogenization result according to the number of fibers is listed in table 3-4. The equation for Δ (%) is $\left| \frac{P_{Halphin-Tsai} - P_{numerical\ average}}{P_{Halphin-Tsai}} \right| \times 100$ where the P can be E or G and the all values of Δ (%) are smaller than 2%. The values are very small as much ignore.

	Analytical result	Numerical result							Δ (%)
		(a)	(b)	(c)	(d)	(e)	(f)	Average	
Number of fibers		1	2	4	8	16	32		
E_L [GPa]	43.10	43.06	43.02	42.93	42.77	42.92	42.76	42.91	0.44
E_T [GPa]	41.58	40.86	40.78	40.84	40.70	40.71	40.66	40.76	1.97
G_{LT} [GPa]	17.42	17.41	17.41	17.42	17.35	17.37	17.34	17.38	0.23

Table 3-4. The comparison between analytical and numerical result according to the number of fibers.
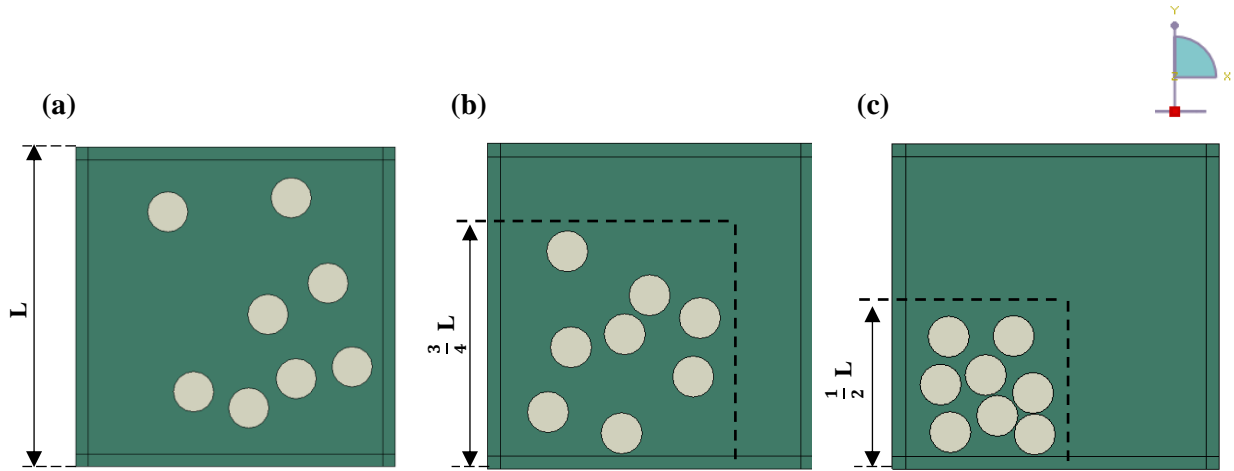
3.7.2 Influence by position of fibers

Figure 3-9. The cross-section of composite according to position of fibers. Fibers are randomly distributed in (a) the total area, (b) $\frac{9}{16}$ **of the total area, and (c) a quarter of the total area.**

I also needed to check the influence by position of fibers. Other variables including volume fraction, properties of fiber and matrix, and size of RVE remained the same as before, while the position of 8 fibers was changed like figure 3-9. In the figure 3-9 (a), fibers were randomly distributed in the total area, while in the figure 3-9 (b) and (c), they are partially distributed. Each result of homogenization is listed in table 3-5. Although, there is a little gap between analytical and numerical result of (a), (b), and (c), the values are very small as much ignore. Therefore, number and position of fibers didn't affect result of homogenization and I selected that the number of fibers for final RVE of AgNWs layer is 32.

	Analytical result	Numerical result				Δ (%)
		(a)	(b)	(c)	Average	
E_L [GPa]	43.10	42.77	42.76	42.76	42.76	0.79
E_T [GPa]	41.58	40.70	40.68	40.69	40.69	2.14
G_{LT} [GPa]	17.24	17.35	17.34	17.32	17.34	0.58
ν_{LT}	0.18	0.17	0.17	0.17	0.17	5.56

Table 3-5. The homogenization result of figure 3-9 according to position of fibers.

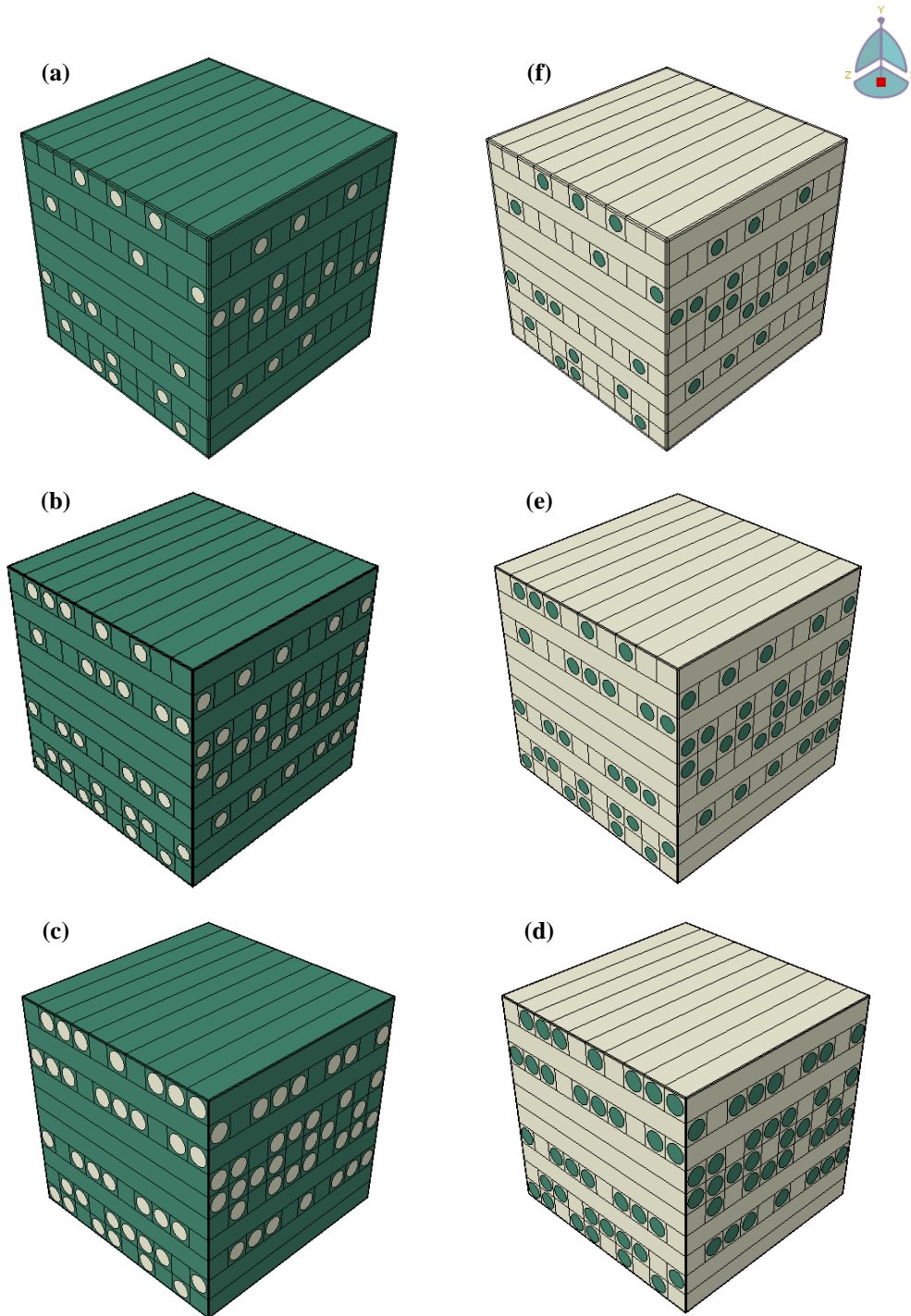# IV. Result and Discussion

4.1 Homogenization result of AgNWs

Figure 4-1. There are RVE modeling according to volume fraction of (a) 10%, (b) 20%, (c) 35%, (d) 65%, (e) 80% and (f) 90%.
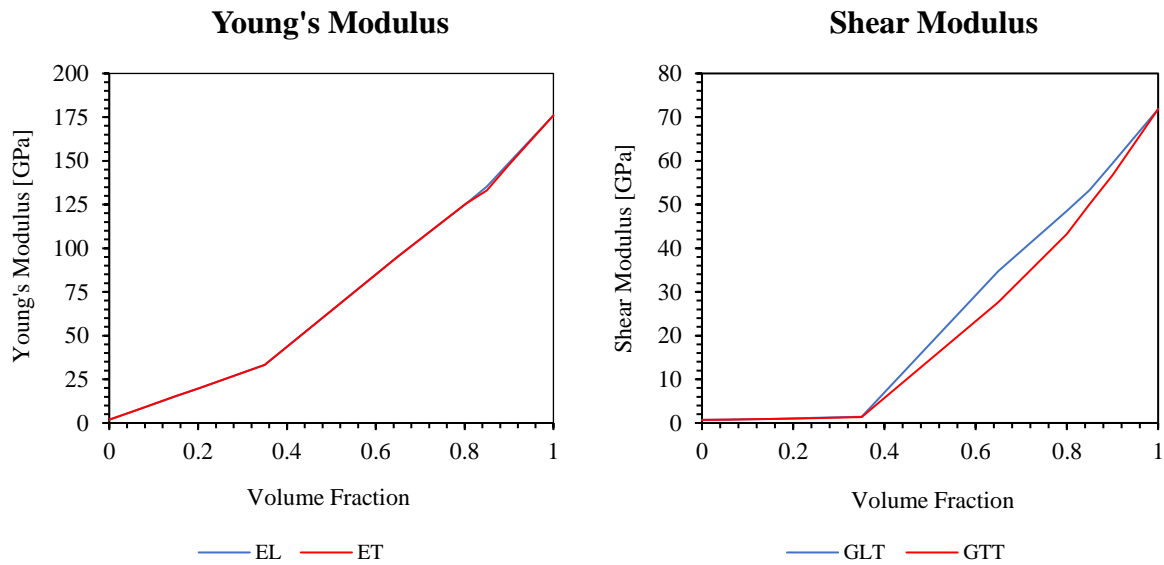
Young's Modulus

Shear Modulus

Figure 4-2. The longitudinal and transversal Young's modulus and shear modulus by homogenization.

Final RVE modeling was made with $10\ mm \times 10\ mm \times 10\ mm$ dimension and fiber which has long length, circle shape and 50% orthogonal pattern. In figure 4-1, the green and ivory colors represent matrix and fiber material, relatively. The elastic properties of them are listed in table 4-1.

I changed the volume fraction of AgNWs from 0% to 100% and checked the homogenization result according to the volume fraction. Figure 4-2 shows the result including longitudinal and transversal Young's modulus and longitudinal and transversal shear modulus. As the volume fraction increases, the values of elastic properties also rapidly increase. Since the final AgNWs layer has 10% volume fraction, the final elastic properties of it are listed in table 4-2.

Elastic properties	AgNWs	PEDOT:PSS
Young's modulus [GPa]	176	1.9
Poisson's ratio	0.225	0.34

Table 4-1. The elastic properties of AgNWs and PEDOT:PSS.

	E_L [GPa]	E_T [GPa]	G_{LT} [MPa]	G_{TT} [MPa]
AgNWs layer	**10.81**	**10.87**	**85.15**	**84.02**

Table 4-2. The homogenization result of AgNWs layer with 10% volume fraction.

4.2 Thickness of AgNWs layer

AgNWs layer embedded PEDOT:PSS and PEDOT:PSS layer were made by spin-coating. First, AgNW solution was coated on a rigid substrate by spin-coating and followed by drying. Next, PEDOT:PSS liquid photopolymer was spin-coated on the AgNW layer and then cured by a commercial ultraviolet (UV). AgNWs was sparsely distributed on the substrate and PEDOT:PSS cover up AgNWs. Total thickness of AgNW layer and PEDOT:PSS layer is 200 nm. Finally, they were peeled off from the substrate. Therefore, the accurate thickness of AgNWs layer was unknown. In this part, I used elastic properties of AgNWs layer with 10% volume fraction and checked the stress distribution in each layer of the OLED according to thickness of AgNWs layer. The values of table 4-3 represent Von-mises and the unit is MPa. The values of Von-mises in each layer are almost the same. Therefore, I checked the thickness of AgNWs layer don't influence on the result and determined 72 nm which is twice of AgNW's diameter.

Thickness of AgNWs layer [nm]	50	72	100	128	150
Al	4497.26	4488.60	4490.13	4486.55	4483.74
PDY-132	435.62	434.78	434.93	434.58	434.31
PEDOT:PSS	121.08	120.87	120.94	120.88	120.83
AgNWs	678.12	676.92	677.25	676.83	676.50
PET	161.69	161.58	161.92	162.05	162.16

Table 4-3. The Von-mises values in each layer according to thickness of AgNWs layer.

4.3 Comparison between stress distribution of OLEDs containing ITO or AgNWs
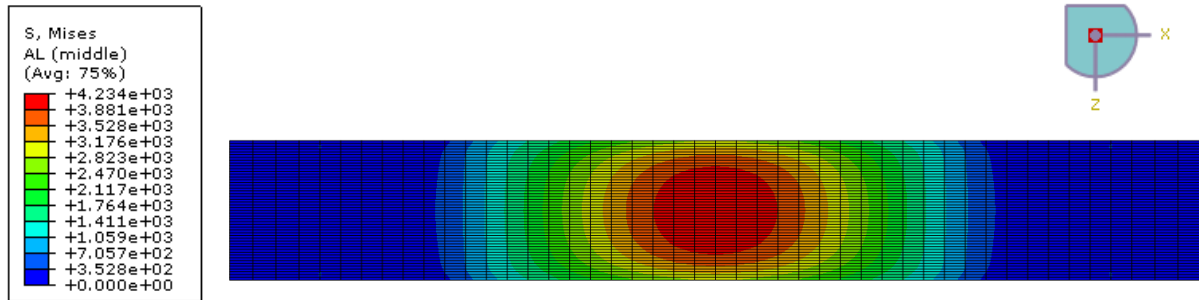

Figure 4-3. Von-mises distribution in Al layer.

As mentioned in the content 1.3 'Reference model of OLEDs', the final OLEDs model contains 5 layers including Al, PDY-132, PEDOT:PSS, anode, and PET substrate and the materials used as anode is ITO or AgNWs with 10% volume fraction. Since elastic properties of AgNWs layer were determined by homogenization in content 4.1 'Homogenization result of AgNWs', I could analyze stress distribution in full modeling designed in content 2 'Full Modeling'. Both final models were subjected to bending test like figure 2-12, and Von-mises distributions in each layer were confirmed by ABAQUS. Since stress is the largest at the center of the shell as shown in figure 4-3, Von-mises values of two final models were measured in there. When the result of the two final models were compared in table 4-4, the values of Von-mises measured at 4 layers exclude anode were almost the same.

Material as anode	Al	PDY-132	PEDOT:PSS	PET
ITO	4462.90	432.33	120.24	161.397
AgNWs	4236.79	410.40	114.16	172.457

Table 4-4. The Von-mises values measured at the center of each layer of two final OLEDs model containing ITO or AgNWs.
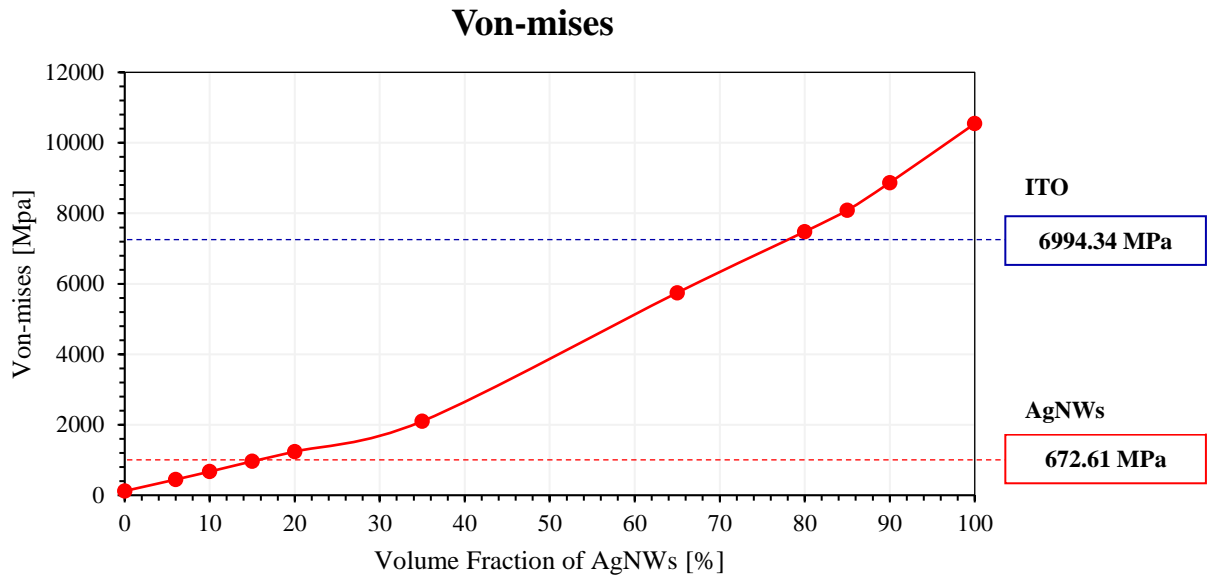
Von-mises

Figure 4-4. The Von-mises in ITO and AgNWs layer under bending test.

In figure 4-4, the values of Von-mises in ITO and AgNWs layer with 10% volume fraction are 672.61 MPa and 6994.34MPa, relatively. The value measured in ITO layer is 10 times larger than the value of Von-mises measured in AgNWs layer and similar with the value of Von-mises of AgNWs layer with 75% volume fraction. Besides the value is very large, ITO has ceramic characteristics and low fracture toughness. Therefore, the reference model including ITO electrode can't withstand the bending test. However, reference model including AgNWs electrode was applied small stress and AgNWs which has high yield stress and PEDOT:PSS which is a conducting polymer doesn't fractured well.

Other stress results listed in table 4-5 also show that stress applied to ITO layer is 10 times to 45 times larger than stress applied to AgNWs layer.

Material as anode	Von-Mises [Mpa]	S11 [MPa]	S22 [MPa]	S12 [MPa]
ITO layer	6994.34	-7849.14	-2273.95	-0.396
AgNWs layer	672.61	-696.54	-50.75	-0.019

Table 4-5. The values of stress measured at the center of the shell including ITO or AgNWs.

In addition to stress distribution, the fracture toughness of ITO and silver are about 2.59 MPa m$^{1/2}$ and 40 MPa m$^{1/2}$ at room temperature. Fracture toughness is used as a failure criterion of material and

represents the resistance of the material to brittle fracture. If fracture toughness value is large, characteristics of the material will usually undergo ductile fracture. The other way, brittle fracture can appear in the material with a low fracture toughness before yielding. The fracture toughness of ITO belongs to a low value, while the fracture toughness of silver belongs to a high value. If ITO is used for flexible OLEDs, it will be easy to break even under small deformation. However, as a result of this thesis, flexible OLEDs made by AgNWs is applied less stress and are not broken under large deformation keeping on high transmittance and low sheet resistant. Therefore, it was confirmed that the AgNWs electrode is superior to the ITO electrode in the aspect of structural and flexural robustness during bending.

V. Reference

1. Jisoo Kim, Yun Seok Nam, Myoung Hoon Song, Hyung Wook Park, 2016, "Large Pulsed Electron Beam Welded Percolation Networks of Silver Nanowires for Transparent and Flexible Electrodes", ACS Appl. Mater. Interfaces 2016, 8, 20938-20945.

2. Antonio Rui Melro, 2011, "ANALYTICAL AND NUMERICAL MODELLING OF DAMAGE AND FRACTURE OF ADVANCED COMPOSITES", The University of Porto, Chapter3, pp. 67-83.

3. Udo Lang, Nicola Naujoks, Jurg Dual, 2009, "Mechanical characterization of PEDOT:PSS thin films", VOL 159, 473-479.

4. Ray Gunawidjaja, Hyunhyub Ko, Chaoyang Jiang, and Vladimir V. Tsukruk, 2007, "Buckling Behavior of Highly Oriented Silver Nanowires Encapsulated within Layer-by-Layer Films", Chem. Mater. 2007, 19, 2007-2015.

5. Seyul Kim, So Yeon Kim, Jeonghun Kim, and Jung Hyun Kim, 2014, "Highly reliable AgNW/PEDOT:PSS hybrid films: efficient methods for enhancing transparency and lowering resistance and haziness", J. Mater. Chem. C, 2014, 2, 5636-5643.

6. Andre Moliton, 2006, "Optoelectronics of Molecules and Polymers", Springer, pp. 201-217.

7. Jinkoo Chung, Joohyeon Lee, Junho Choi, Chanyoung Park, Jaekook Ha, Hokyoon Chung, Sang Soo Kim, "Transparent AMOLED Display Based on Bottom Emission Structure", OLED R&D Center, Samsung Mobile Display Co., LTD.

8. Sanggil Nam, Myungkwan Song, Dong-Ho Kim, Byungjin Cho, Hye Moon Lee, Jung-Dae Kwon, Sung-Gyu Park, Kee-Seok Nam, Yongsoo Jeong, Se-Hun Kwon, Yun Chang Park, Sung-Ho Jin, Jae-Wook Kang, Sungjin Jo, Chang Su Kim, 2014, "Ultrasmooth, extremely deformable and shape recoverable Ag nanowire embedded transparent electrode", SCIENTIFIC REPORTS 6:36475.

9. Srihari Kurukuri, 2005, "Homogenization of Damaged Concrete   Meso-structures using Representative Volume Elements – Implementation and Application to Slang", Bauhaus–University Weimar Germany, pp. 48-61.

10. Fan Ye, Hu Wang, 2017, "A simple Python code for computing effective properties of 2D and 3D representative volume element under periodic boundary conditions", Hunan University, Changsha 410082, P.R. China.

11. Weidong Wu, Joseph Owino, Ahmed Al-Ostaz, Liguang Cai, 2014, "Applying Periodic Boundary Conditions in Finite Element Analysis", University of Tennessee Chattanooga and Mississippi.

12. Yonghee Jang, Jihoon Kim, Doyoung Byun, 2013, "Invisible metal-grid transparent electrode prepared by electrohydrodynamic (EHD) jet printing", J. Phys. D: Appl. Phys. 46 (2013) 155103 (5pp).

13. Won-Yong Jin, Riski Titian Ginting, Keum-Jin Ko and Jae-Wook Kang, 2016, "Ultra-Smooth, Fully SolutionProcessed Large-Area Transparent Conducting Electrodes for Organic Device", SCIENTIFIC REPORTS